

Title

Intestinal transit amplifying cells require METTL3 for growth factor signaling and cell survival

Authors

Charles H. Danan^{1,2,3}, Kaitlyn E. Naughton¹, Katharina E. Hayer^{4,5,6}, Sangeevan Vellappan^{7,8,9}, Emily A. McMillan¹, Yusen Zhou^{1,4}, Rina Matsuda^{3,10}, Shaneice K. Nettleford¹, Kay Katada^{1,3}, Louis R. Parham^{1,3}, Xianghui Ma¹, Afrah Chowdhury¹, Benjamin J. Wilkins⁶, Premal Shah^{8,9}, Matthew D. Weitzman^{3,5,6}, Kathryn E. Hamilton^{1,3,11*}

Affiliations

¹Division of Gastroenterology, Hepatology, and Nutrition; Department of Pediatrics; Children's Hospital of Philadelphia; Perelman School of Medicine, University of Pennsylvania, Philadelphia, PA, 19104, USA;

²Medical Scientist Training Program, Perelman School of Medicine, University of Pennsylvania, Philadelphia, PA, 19104, USA;

³Perelman School of Medicine, University of Pennsylvania, Philadelphia, PA, 19104, USA;

⁴Department of Biomedical and Health Informatics, The Children's Hospital of Philadelphia, Philadelphia, PA, 19104, USA

⁵Division of Protective Immunity, Children's Hospital of Philadelphia, Philadelphia, PA, 19104, USA;

⁶Department of Pathology and Laboratory Medicine, Perelman School of Medicine; University of Pennsylvania, Philadelphia, PA, 19104, USA;

⁷Waksman Institute of Microbiology, Rutgers University, Piscataway, NJ, 08854, USA;

⁸Department of Genetics, Rutgers University, Piscataway, NJ, 08854, USA;

⁹Human Genetics Institute of New Jersey, Piscataway, NJ, 08854, USA;

¹⁰Department of Pathobiology, School of Veterinary Medicine, University of Pennsylvania, Philadelphia, PA, 19104, USA;

¹¹Institute for Regenerative Medicine, University of Pennsylvania, Philadelphia, PA, 19104, USA.

*Corresponding Author

Kathryn E. Hamilton, PhD
903 Abramson Research Building
Children's Hospital of Philadelphia
3615 Civic Center Blvd.
Philadelphia, PA 19104, USA
267-426-5266
hamiltonk1@chop.edu

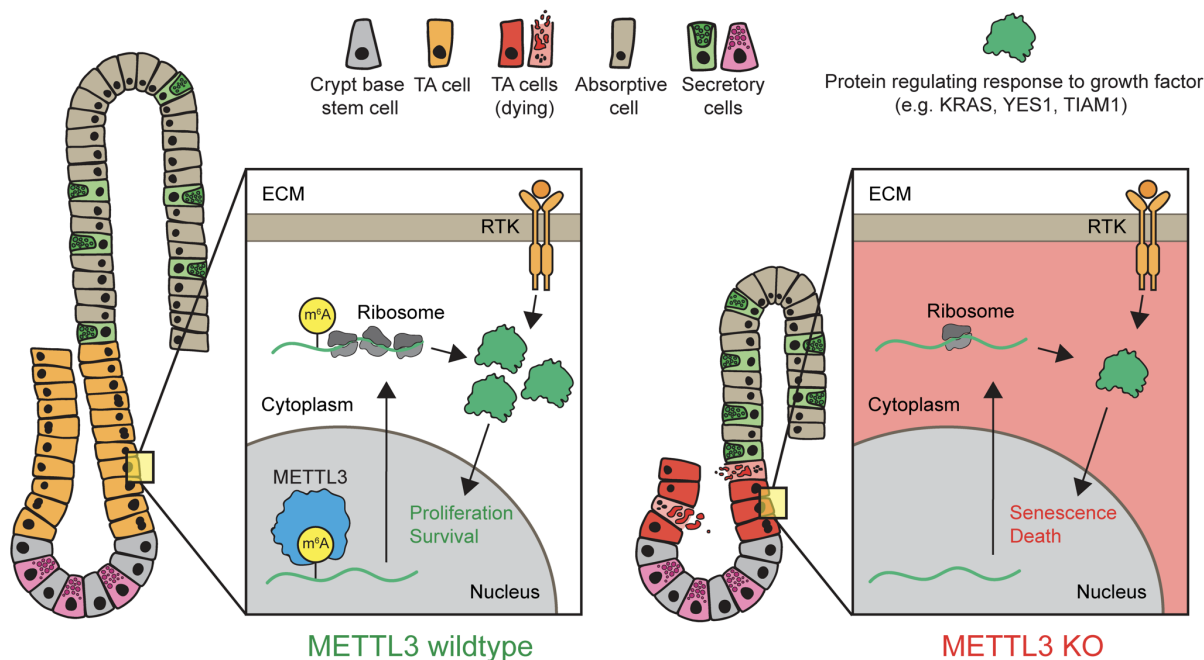
Conflict-of-interest statement

Premal Shah is a member of the Scientific Advisory Board of Trestle Biosciences and is Director at Ananke Therapeutics. All other authors declare they have no competing interests.

Abstract

Intestinal epithelial transit amplifying cells are essential stem progenitors required for intestinal homeostasis, but their rapid proliferation renders them vulnerable to DNA damage from radiation and chemotherapy. Despite their critical roles in intestinal homeostasis and disease, few studies have described genes that are essential to transit amplifying cell function. We report that the RNA methyltransferase, METTL3, is required for survival of transit amplifying cells in the murine small intestine. Transit amplifying cell death after METTL3 deletion was associated with crypt and villus atrophy, loss of absorptive enterocytes, and uniform wasting and death in METTL3-depleted mice. Sequencing of polysome-bound and methylated RNAs in enteroids and in vivo demonstrated decreased translation of hundreds of unique methylated transcripts after METTL3 deletion, particularly transcripts involved in growth factor signal transduction such as *Kras*. Further investigation confirmed a relationship between METTL3 and *Kras* methylation and protein levels in vivo. Our study identifies METTL3 as an essential factor supporting the homeostasis of small intestinal tissue via direct maintenance of transit amplifying cell survival. We highlight the crucial role of RNA modifications in regulating growth factor signaling in the intestine with important implications for both homeostatic tissue renewal and epithelial regeneration.

Graphical Abstract



MAIN TEXT

Introduction

The intestinal epithelium digests and absorbs nutrients, protects against pathogen invasion, and regulates interactions between mucosal immune cells and the gut lumen (1). These essential functions are made possible by the continuous renewal of differentiated intestinal epithelial cells (2). Epithelial renewal begins at the intestinal crypt base, where intestinal stem cells expressing the Wnt target gene, LGR5, initiate differentiation and migrate up the crypt wall. As they move up the crypt wall, LGR5⁺ stem cells differentiate into intestinal stem progenitors known as transit amplifying (TA) cells (2). TA cells rapidly undergo successive cycles of proliferation to generate the bulk of intestinal epithelium. While existing research emphasizes the role of LGR5⁺ stem cells in tissue renewal, TA cells are the primary site of intestinal epithelial proliferation and differentiation, and they produce the majority of differentiated epithelium (3, 4). Rapid proliferation is the central defining feature of TA cells, and it renders them particularly vulnerable to DNA damaging agents such as chemotherapeutics and radiation therapy (5–7). These routine cancer treatments cause chemotherapy-induced gastrointestinal toxicity (CIGT) and radiation induced gastrointestinal syndrome (GIS), which together affect >80% of cancer patients. CIGT and GIS are debilitating pathologies with limited treatment options (8–10). One potential therapeutic avenue would be the development of drugs that protect the TA cells preferentially damaged by these common cancer therapies. However, despite their critical roles in intestinal homeostasis and disease, factors that maintain survival and proliferation of TA cells remain inadequately defined compared to the extensive study of LGR5⁺ stem cells.

Novel approaches are needed to identify factors that specifically regulate TA cell function. While numerous studies have defined transcriptional control of intestinal stem cells, post-transcriptional regulation of intestinal epithelial homeostasis is only beginning to be understood. Recent research points to important roles for the RNA modification, N6-methyladenosine (m⁶A), in intestinal crypts (11–15). N6-methyladenosine is the most common covalent modification of RNA, occurring on approximately 25% of mRNA transcripts (16, 17). It acts by recruiting RNA-binding proteins that affect mRNA fate, predominantly stability and translation. (18). Global m⁶A methylation patterns in the epithelium can shift with microbial and nutrient contents of the gut and m⁶A-binding proteins have been implicated in intestinal regeneration and

the pathogenesis of inflammatory bowel disease (IBD) (11, 13, 15, 19, 20). These studies suggest critical roles for m⁶A in integrating environmental cues with homeostatic and regenerative processes in the intestinal epithelium.

Despite advances in the study of m⁶A in the gut, the effect of global depletion of m⁶A in the intestinal epithelium remains unclear and incomplete, particularly in the small intestine. A highly conserved m⁶A “writer” complex installs m⁶A co-transcriptionally in the nucleus of eukaryotic cells. At the core of this complex are the writer proteins Methyltransferase-like 3 and 14 (METTL3 and METTL14) (18). Although METTL3 is the catalytic subunit, both METTL3 and METTL14 are thought to be essential for the methylating activity of the complex (21, 22), and both METTL proteins are deleted interchangeably to define the role of m⁶A in specific tissue or cell types. Recent studies reported essential functions for METTL14 in the survival of LGR5⁺ stem cells in the colon, with complete sparing of the small intestine (23, 24). In contrast, another very recent study found that METTL3 deletion caused defects in LGR5⁺ stem cells in the small intestine (25). However, in the case of METTL3 deletion, rescue of LGR5⁺ stem cell survival could not rescue tissue homeostasis. Therefore, the critical defect in METTL3-depleted epithelium remains unclear.

In contrast to previous reports emphasizing dysfunction of LGR5⁺ stem cells, we found that METTL3 deletion induced profound cell death predominantly in small intestinal transit amplifying cells. Disruption of the TA zone was associated with crypt and villus atrophy and widespread reduction in absorptive enterocytes, ultimately resulting in the death of METTL3-depleted mice. Sequencing of m⁶A-modified RNA in vivo and polysome-bound RNA in METTL3-depleted enteroids revealed decreased translation efficiency for methylated transcripts critical to growth factor signaling, including master growth regulator and proto-oncogene, *Kras*. Additional investigation confirmed a link between METTL3 and *Kras* methylation and protein expression. Our data identify METTL3 as an essential regulator of intestinal transit amplifying cell survival via direct support of growth factor signaling, including KRAS expression. By identifying epitranscriptomic regulation as an indispensable process within TA cells, we highlight the importance of an emergent gene regulatory mechanism in this critical but poorly understood cell type.

Results

Intestinal epithelial METTL3 deletion results in complete growth failure and mortality

To determine the role of METTL3 in intestinal epithelial development and homeostasis, we paired *Mettl3^{fllox/fllox}* mice with the pan-intestinal-epithelial *Villin-Cre* (*Mettl3^{VilCreΔ/Δ}*) or its tamoxifen inducible counterpart, *Villin-CreERT2* (inducible *Mettl3^{VilCreERT2Δ/Δ}*). First, we examined *Mettl3^{VilCreΔ/Δ}* mice, which had constitutive Cre activation in the small intestinal and colonic epithelium beginning at embryonic day 12.5 (26). These mice were born with Mendelian distribution (X^2 $n=79$ $p>0.74$) and appeared grossly normal at postnatal day 14, as previously described (27). However, from postnatal day 21 to 28, *Mettl3^{VilCreΔ/Δ}* mice lost ~20% starting body weight while controls gained ~40% (Figure 1A). Body condition and weight loss in *Mettl3^{VilCreΔ/Δ}* mice required euthanasia of 70% of mice between postnatal day 16-29 (Figure 1, B-D). To determine whether this phenotype was development-specific, we next examined inducible *Mettl3^{VilCreERT2Δ/Δ}* mice injected with tamoxifen at 8 weeks of age (Figure 2A). After their final tamoxifen injection, inducible *Mettl3^{VilCreERT2Δ/Δ}* mice exhibited an average daily weight loss of ~2.5% (Figure 2B). Within 10 days, almost all mice experienced critical (>20%) weight loss requiring euthanasia (Figure 2, B and C). These data demonstrate a requirement of METTL3 for growth and survival during the postnatal period and adulthood.

METTL3 deletion induces small intestinal crypt and villus atrophy

We next examined the intestinal pathology of *Mettl3^{VilCreΔ/Δ}* and inducible *Mettl3^{VilCreERT2Δ/Δ}* mice to determine the cause of their severe growth failure and mortality. We assessed *Mettl3^{VilCreΔ/Δ}* mice at postnatal day 29 and inducible *Mettl3^{VilCreERT2Δ/Δ}* mice at nine days post-tamoxifen injection since at this timepoint both cohorts exhibited daily weight loss and >50% of mice met the humane endpoints for euthanasia (see Methods). Western blot, in situ staining, and m⁶A dot blot confirmed depletion of METTL3 and m⁶A in the intestinal epithelium (Supplemental Figure 1, A-C, and Supplemental Figure 2, A and B). We also observed commensurate depletion of METTL14 in METTL3 knockout tissues, which is consistent with previous reports demonstrating stabilization of METTL14 by METTL3 (Supplemental Figures 1A and 2A) (28, 29). Using a composite histopathological score in both METTL3 knockout models, we noted histological changes throughout the small intestine and colon with only the distal colon being relative spared (Figure 1, E-G, and Figure 2, D-F). Defects were most severe in the distal small intestine, where we observed widespread crypt atrophy alongside villus shortening. After METTL3 knockout, villi in the jejunum averaged only ~30% of their normal length (Supplemental Figure 1D and Supplemental Figure 2C). Many

distal small intestinal crypts also degenerated after METTL3 deletion, although we noted occasional hypertrophic regenerative crypts (Figure 1E and Figure 2D). Since METTL3 and METTL14 knockouts are generally considered equivalent, our findings of small intestinal destruction with distal colonic sparing were striking and unexpected given previous studies indicating METTL14 deletion spares the small intestine but induces severe distal colonic defects (23, 24). These data demonstrate that intestinal epithelial METTL3 is required for both the postnatal development and adult maintenance of full-length crypt and villus structures, particularly in the distal small intestine.

METTL3 is required for intestinal epithelial proliferation and survival

To determine the origins of crypt and villus atrophy, we next evaluated proliferation and apoptosis in *Mettl3*^{VilCreΔ/Δ} and inducible *Mettl3*^{VilCreERΔ/Δ} mice. Since histological changes were most severe in the distal small intestine, we focused on Ki67 and TUNEL staining in this tissue. In METTL3 knockout epithelium, atrophied crypts previously observed by H&E exhibited drastically reduced Ki67 staining. Where control crypts had an average of ~30 Ki67+ cells/crypt, atrophic METTL3 depleted crypts often exhibited fewer than 10 Ki67+ cells (Figure 1H and Figure 2G). We also observed some hyperproliferative crypts in both deletion models (>45 Ki67+ cells), although in inducible *Mettl3*^{VilCreERΔ/Δ} mice, these were frequently METTL3+ by immunofluorescence (Supplemental Figure 2D), suggesting small areas of incomplete genetic deletion. Thus, we elected to not quantify these hyperproliferative crypts. We also identified a >10-fold increase in the mean number of TUNEL positive cells in both *Mettl3*^{VilCreΔ/Δ} and inducible *Mettl3*^{VilCreERΔ/Δ} mice, demonstrating extensive cell death throughout the villus and crypt (Figure 1I and Figure 2H). These data suggest that both disrupted proliferation and cell survival contributed to epithelial defects in *Mettl3*^{VilCreΔ/Δ} and inducible *Mettl3*^{VilCreERΔ/Δ} mice.

METTL3 is required for absorptive enterocyte maturation

To evaluate etiologies of weight loss and epithelial distortion in METTL3 knockout mice, we examined the distribution of differentiated epithelial cells. The differentiated intestinal epithelium comprises secretory and absorptive lineages, which both play essential roles in intestinal homeostasis. Secretory cell depletion can promote epithelial defects due to important roles in producing mucus, antimicrobial

compounds, and stem cell niche factors (30, 31). However, even in areas of severe epithelial distortion, we observed maintenance of MUC2+ goblet cells with only minor, inconsistent reductions in LYZ+ Paneth cells and CHGA+ enteroendocrine cells (Figure 1, J-L, and Figure 2, I-K). Alcian blue staining corroborated these findings by indicating mucus production was also maintained in the small intestine, though we did observe reductions in mucus in the proximal colon (Supplemental Figure 1E and Supplemental Figure 2E). In contrast to modest changes in secretory lineages, we observed a dramatic decrease in expression of absorptive enterocyte marker, alkaline phosphatase. Both *Mettl3*^{VilCreΔ/Δ} mice and inducible *Mettl3*^{VilCreERΔ/Δ} mice exhibited ~50% less alkaline phosphatase staining in the distal small intestine, suggesting dramatic loss of absorptive enterocytes (Figure 1M and Figure 2L). This effect was strongest in areas of severe villus shortening, where we observed almost no alkaline phosphatase staining. Taken together, we found general maintenance of secretory cells but a dramatic reduction in mature absorptive enterocytes in *Mettl3*^{VilCreΔ/Δ} mice and inducible *Mettl3*^{VilCreERΔ/Δ} mice. We propose that the resulting loss of absorptive capacity may underlie wasting in these METTL3 knockout mice.

Alternative METTL3 deletion recapitulates small intestinal defects

We performed the above experiments in inducible *Mettl3*^{VilCreERΔ/Δ} mice using *loxP* sites spanning nine exons of the *Mettl3* locus (Supplemental Figure 3A) (32). This large deletion resulted in some reduction of recombination efficiency in the distal colon and to a lesser degree, the small intestine (Supplemental Figure 2, B and D). We were also surprised to identify a small intestinal defect after METTL3 deletion, because m⁶A-depletion via METTL14 deletion produced no small intestinal phenotype in recent publications (23, 24). To address these concerns, we tested a second METTL3 deletion model with *LoxP* sites spanning only exon 4 (*Mettl3*^{VilCreERΔ2/Δ2}, Supplemental Figure 3, A and B) (33). Inducible *Mettl3*^{VilCreERΔ2/Δ2} mice demonstrated efficient deletion of METTL3 in all targeted tissues (Supplemental Figure 3C). In this additional model, we confirmed rapid weight loss and mortality, hypo- and hyper-plastic crypts, preservation of secretory goblet and Paneth cells, and absent distal colonic defects (Supplemental Figure 3, D-G). These data further support the conclusion that METTL3 is essential for small intestinal homeostasis.

Intestinal defects with METTL3 deletion are independent of intestinal microbiota

Microbial translocation and inflammatory activation are common causes of morbidity and mortality in mice with intestinal epithelial defects. Furthermore, we observed modest increases in the number of inflammatory immune cells in the intestinal mucosa of METTL3 depleted mice (Figure 1G and Figure 2F). We therefore examined sera of inducible *Mettl3*^{VilCreERΔ/Δ} mice for elevated inflammatory cytokines nine days post final tamoxifen injection, when mice appeared the most grossly ill as described above. Intriguingly, there was no significant difference in serum cytokine markers TNF-α, IL-6, IL-1α, IL-1β, IL-10, IL-12 or IFN-γ in *Mettl3*^{VilCreERΔ/Δ} mice compared to controls (Figure 3A). Additionally, spleen size—often positively correlated with degree of whole-body inflammation—was reduced (Figure 3B), and small intestine and colon lengths—often reduced in inflammatory conditions—were unchanged at this same timepoint (Figure 3, C and D). Taken together, these data suggested a non-inflammatory etiology to morbidity and mortality in *Mettl3*^{VilCreERΔ/Δ} mice.

Despite no overt inflammatory pathology, the contribution of facility-specific microbiota is a common concern in the evaluation of intestinal phenotypes. We also questioned whether the microbiota contributed to the surprising difference in small intestinal phenotypes between METTL3 and previously described METTL14 knockout intestinal epithelium (23, 24). Therefore, we depleted the microbiota in *Mettl3*^{VilCreERΔ/Δ} mice by adding an antibiotic cocktail to their drinking water beginning one week before tamoxifen injection (Figure 3E). Quantitative PCR of genomic 16S rRNA confirmed ~1000-fold depletion of luminal bacteria (Figure 3F). There was no change in weight loss or mortality in microbiota depleted *Mettl3*^{VilCreERΔ/Δ} mice compared to those on normal drinking water (Figure 3, G and H). Histological abnormalities also persisted in microbiota depleted *Mettl3*^{VilCreERΔ/Δ} mice (Figure 3I). Taken together, these data suggest minimal contribution of inflammation or microbiota to the gross and histological defects seen in *Mettl3*^{VilCreERΔ/Δ} mice. Rather, they further support a model in which loss of absorptive enterocytes diminishes digestive capacity leading to weight loss and mortality in these mice.

METTL3 deletion immediately triggers transit amplifying cell death

Inducible *Mettl3*^{VilCreERΔ/Δ} mice displayed a complex set of histological phenotypes, including adjacent hypertrophic and atrophic crypts and scattered villus and crypt cell death. Some of these changes may be reactive, secondary changes rather than immediately downstream of METTL3 depletion. We

therefore examined inducible *Mettl3*^{VilCreERΔ/Δ} mice two days after the final tamoxifen injection- the earliest timepoint at which we confirmed METTL3 deletion by immunoblot and in situ staining (Figure 4A and Supplemental Figure 2, A and B). At this early deletion timepoint, *Mettl3*^{VilCreERΔ/Δ} mice demonstrated a ~30% increase in crypt height in the small intestine (Figure 4B). This change was associated with increased numbers of Ki67+ cells (Figure 4C) and increased expression of transcripts associated with stem cells and stem progenitors, including key stem cell marker *Lgr5* (Figure 4D). In contrast, we observed profound TA cell death in inducible *Mettl3*^{VilCreERΔ/Δ} mice at this same early timepoint. The mean number of TUNEL+ foci per crypt was elevated >20-fold in *Mettl3*^{VilCreERΔ/Δ} crypts compared to controls (Figure 4E). Strikingly, almost all TUNEL+ foci in *Mettl3*^{VilCreERΔ/Δ} small intestine were in the TA zone, located between the crypt base and the crypt-villus junction. We quantified TUNEL+ staining in the crypt base, TA zone, and villus epithelium and found 3-fold higher cell death rates in the TA zone compared to the crypt base (Figure 4F). These data suggest that the initial defect in inducible *Mettl3*^{VilCreERΔ/Δ} mice is widespread transit amplifying cell death.

METTL3 deletion causes growth arrest and death in intestinal enteroids

We next wanted to establish an epithelial-specific model for examining the kinetics and mechanism of cell death in *Mettl3*^{VilCreERΔ/Δ} mice. We therefore generated 3D organoids from small intestinal crypts (enteroids) and colonic crypts (colonoids) of *Mettl3*^{VilCreERΔ/Δ} and *Mettl3*^{flox/flox} mice and treated with 4-hydroxytamoxifen (4-OHT) in vitro to induce METTL3 deletion (Figure 5A) (34). We first monitored gross cell death in enteroids and colonoids. We defined dead organoids as those with a complete opaque appearance, leaking of dead cell debris, and absent growth over the subsequent 24 hours. Nearly all *Mettl3*^{VilCreERΔ/Δ} enteroids and proximal colonoids died within 5 days post 4-OHT withdrawal. Mirroring our results in vivo, only distal colonoids from *Mettl3*^{VilCreERΔ/Δ} mice survived 4-OHT treatment, where immunoblotting confirmed deletion of METTL3 (Figure 5, B-D). To map the chronology of enteroid growth and survival after METTL3 deletion, we examined ileal enteroids, which had the greatest rate of death. We measured ileal enteroid size and death daily after 4-OHT treatment of *Mettl3*^{VilCreERΔ/Δ} and control *Villin-CreERT2* enteroids. Enteroids appeared grossly normal in the first two days after 4-OHT withdrawal. At day 3, *Mettl3*^{VilCreERΔ/Δ} enteroids exhibited growth arrest concurrent with increased death, ultimately resulting in complete death by five days post 4-OHT (Figure 5, E-G). In summary, *Mettl3*^{VilCreERΔ/Δ} enteroids and

colonoids recapitulated tissue-region-specific cell death phenotypes observed in vivo. These data confirmed that cell death phenotypes after METTL3 deletion were epithelial-cell-autonomous; they also established enteroids as an effective model of in vivo pathologies for further mechanistic investigation.

Catalytic inactive METTL3 does not rescue death of METTL3 depleted enteroids

Given that METTL3 deletion led to small intestinal epithelial death in vivo and in vitro, but depletion of the essential methyltransferase co-factor METTL14 has been previously reported to have no effect on small intestinal homeostasis (23, 24), we hypothesized that METTL3 might support intestinal epithelial survival through a non-catalytic mechanism. To test this, we reintroduced a non-catalytic METTL3 (DPPW³⁹⁵⁻³⁹⁸ to APPA³⁹⁵⁻³⁹⁸) (35) to *Mettl3*^{VilCreERΔ/Δ} ileal enteroids using a lentiviral construct (METTL3^{Δcat}). Western and dot blot confirmed rescue of METTL3 expression, but not m⁶A, in *Mettl3*^{VilCreERΔ/Δ} + METTL3^{Δcat} enteroids (Supplemental Figure 4, A and B). However, *Mettl3*^{VilCreERΔ/Δ} + METTL3^{Δcat} enteroids still died by day 5 post 4-OHT, similar to negative controls (Supplemental Figure 4, C and D). Conversely, an identical lentiviral construct expressing wildtype METTL3 (METTL3^{wt}) restored m⁶A levels and completely rescued death of *Mettl3*^{VilCreERΔ/Δ} enteroids (Supplemental Figure 4, A-D). Finally, we considered previous reports indicating that METTL3 may act independently of METTL14 as a non-catalytic cytoplasmic regulator of protein translation (36–38). However, we observed exclusively nuclear staining of endogenous METTL3 in ileal enteroids, likely precluding this possibility (Supplemental Figure 4E). Together, these data suggest that small intestinal epithelium requires the nuclear, catalytic activity of METTL3 for homeostatic function.

METTL3 deletion triggers global downregulation of translational efficiency

Previous studies indicate that m⁶A induces global changes in mRNA abundance and translational efficiency (13, 39, 40). To identify METTL3 targets that may mediate phenotypes observed in vivo and in vitro, we sequenced total RNA and polysome-bound RNA to assay global changes in RNA abundance and translation after METTL3 deletion (Supplemental Data 1 and 2). Quality control analysis of polysome-bound RNA revealed read depth, read length, and inter-replicate reproducibility consistent with field standards for polysome profiling (Supplemental Figure 5, A-D). To accurately estimate translation, we compared the ratio of polysome-bound RNA to total mRNA for each transcript to generate the translational efficiency (“TE”) of

each transcript (11, 41). Since METTL3 modifies thousands of transcripts with pleiotropic effects, we elected to analyze *Mettl3*^{VilCreERΔ/Δ} ileal enteroids 72 hours after initiating 4-OHT treatment to detect the changes most proximal to METTL3 deletion but prior to widespread cell death. Comparing the approximately 25,000 transcripts detected in both data sets, METTL3 deletion impacted more transcripts at the level of RNA translation (2,124 transcripts) than RNA abundance (1,231 transcripts) (Figure 6A and Supplemental Figure 6A). Averaging all 2,124 transcripts with significant changes in TE, the predominant effect of METTL3 deletion was reduced TE, with 1,747 transcripts exhibiting reduced TE and 377 with increased TE. Taken together, there was a mean decrease in TE of 39% across all differentially translated transcripts in *Mettl3*^{VilCreERΔ/Δ} enteroids compared to controls (Figure 6A). These data suggest that METTL3 broadly supports translation in the small intestinal epithelium.

METTL3 deletion downregulates translation of methylated transcripts regulating growth factor signaling

We next performed m⁶A immunoprecipitation and sequencing (m⁶A-seq) in wildtype mouse crypts in vivo to define putative direct targets of METTL3 (16, 17, 42). m⁶A-seq yielded 13,763 m⁶A peaks within 7,882 unique transcripts (Supplemental Data 3). Peaks were distributed across the coding sequence and 3' untranslated region, with the highest accumulation at the stop codon, consistent with previous reports (Supplemental Figure 7A) (16, 17). We also saw expected patterns of m⁶A enrichment in positive and negative control transcripts (Supplemental Figure 7B). We superimposed m⁶A-seq data onto translational efficiency data and found that of the 1,747 transcripts with decreased TE after METTL3 deletion, 368 transcripts contained at least one m⁶A peak. These 368 m⁶A-modified transcripts had a median TE decrease of 50% after METTL3 deletion (Figure 6B). By comparison, only 165 m⁶A-modified transcripts had *any* change in RNA abundance after METTL3 deletion, and the magnitude of these changes was approximately half that seen in the TE analysis (Supplemental Figure 6, B and C). Because we observed more changes in RNA translation than abundance after METTL3 deletion, we chose to focus our remaining analysis on changes in translational efficiency. We next used Gene Ontology Biological Process (GOBP) gene sets to conduct pathway enrichment analysis on these 368 methylated transcripts with downregulated TE after METTL3 deletion. We observed the most significant enrichment in transcripts associated with

growth factor signaling cascades (Figure 6C). We observed broadly reduced TE in growth factor associated transcripts (Figure 6D). Notably, the largest magnitude reduction in TE was for *Kras*, an essential intestinal proto-oncogene that promotes intestinal epithelial proliferation and survival (43). Taken together, sequencing of polysome-bound and m⁶A-modified mRNA indicate that METTL3 deletion downregulates translation of methylated transcripts supporting growth factor signaling including *Kras*.

METTL3 deletion reduces *Kras* methylation and protein levels and induces cellular senescence

We further explored the putative relationship between METTL3 and KRAS expression by examining m⁶A modification of the *Kras* transcript. Our m⁶A-seq data indicated enriched m⁶A density across the *Kras* gene body, including both UTRs (Figure 7A). However, to our knowledge, previous literature had never identified m⁶A methylation of *Kras*. To verify m⁶A-seq peaks on the *Kras* transcript and determine their dependence on METTL3 expression, we performed m⁶A-RNA-immunoprecipitation-qPCR (m⁶A-RIP-qPCR) in crypt-enriched lysates from *Mettl3^{flox/flox}* and *Mettl3^{VilCreERΔ/Δ}* mice three days after final tamoxifen injection. We found significant enrichment of m⁶A in all *Kras* mRNA regions using four unique qPCR probes targeting the *Kras* 5' UTR, CDS exons 1-2, CDS exons 3-4A, and 3' UTR (Figure 7, B-E). However, close examination of our data suggested that the true m⁶A peak occupied the 3' UTR only. Of the four regions sampled, m⁶A enrichment only appeared dependent on METTL3 expression in CDS exons 3-4A and the 3' UTR (Figure 7, D and E). Of these two regions, only the 3' UTR demonstrated clear m⁶A enrichment in the m⁶A-seq (Figure 7A). The low resolution of the m⁶A-RIP-qPCR (~200-300 nt) could explain why we observed m⁶A-enrichment in CDS exons 3-4A. The m⁶A enrichment in the 5' UTR and neighboring CDS exons 1-2 (Figure 7, B and C) likely represent N6,2'-O-dimethyladenosine (m⁶Am), a terminal modification added to the 5' mRNA cap independent of METTL3; m⁶Am is an established off-target of m⁶A antibodies (44). These data support our original finding that METTL3 methylates *Kras* in the 3'UTR.

We next examined how methylation of *Kras* impacts its expression in vivo. Although METTL3 deletion did not significantly impact *Kras* transcript abundance via qPCR, we observed a decrease in KRAS protein in crypt-enriched lysates from *Mettl3^{VilCreERΔ/Δ}* mice compared to controls (Figure 7, F and G). To further validate our polysome sequencing data in vivo, we also examined protein expression levels of other top downregulated genes of interest. We confirmed decreases in YES1 (src family kinase and proto-

oncogene) and SEC13 (member of the nuclear pore complex implicated in mRNA export) but not UBE1 (primary enzyme in conjugation of ubiquitin) (45–47) (Figure 7G). Finally, to support our model of reduced KRAS expression, we examined the distal small intestine of inducible *Mettl3*^{VilCreERΔ/Δ} mice for levels of key downstream target, phosphorylated ERK. Control crypts averaged between 30 to 40 p-ERK positive cells, predominantly in the TA zone. By contrast, about 50% of atrophic small intestinal crypts in *Mettl3*^{VilCreERΔ/Δ} mice had fewer than five p-ERK positive cells per crypt after deletion of METTL3 (Figure 7H). Taken together, these data suggest that METTL3 promotes KRAS expression and signaling without impacting *Kras* transcript levels, providing further mechanistic support for METTL3 as a post-transcriptional regulator of *Kras* translation.

KRAS is a key mediator of epidermal growth factor (EGF) signaling in epithelial cells (43). Loss of mitogenic signals such as EGF induces cell cycle arrest and senescence in proliferative cells (48). We therefore assessed senescence in the crypts of inducible *Mettl3*^{VilCreERΔ/Δ} mice by staining for p21, γ-H2AX, and β-galactosidase two days after final tamoxifen injection. *Mettl3*^{VilCreERΔ/Δ} crypts demonstrated elevated p21, γ-H2AX, and β-galactosidase compared to controls, particularly in the TA zone (Figure 7, I-K). Dying *Mettl3*^{VilCreERΔ/Δ} enteroids also exhibited strong β-galactosidase staining compared to controls (Figure 7L). One potential caveat to these findings is the possibility of toxic combined effects of CreERT2 and tamoxifen in intestinal stem cells within a week of tamoxifen exposure (49). To address this, we evaluated p21 and γ-H2AX in tamoxifen-treated *Villin-CreERT2* control mice at the same timepoint. Both p21 and γ-H2AX were significantly increased in *Mettl3*^{VilCreERΔ/Δ} mice compared to *Villin-CreERT2* controls (Supplemental Figure 8, A and B). Although we propose that KRAS downregulation is not the sole event responsible for the death of METTL3 KO epithelium, we examined whether overexpression of KRAS could rescue death of METTL3 KO enteroids to definitively determine the role of KRAS expression. We introduced vectors expressing either KRAS or constitutively active KRAS^{G12D} to *Mettl3*^{VilCreERΔ/Δ} enteroids and induced METTL3 KO. Unsurprisingly, neither KRAS nor constitutively active KRAS^{G12D} could rescue *Mettl3*^{VilCreERΔ/Δ} enteroids (Supplement Figure 9, A-C). Taken together, these data support the hypothesis that loss of proteins supporting growth factor signaling, including but not limited to KRAS, triggers cellular senescence in the crypt TA zone after METTL3 deletion.

Discussion

Our collective findings examining METTL3 deletion in the intestinal epithelium in vivo and in vitro support a model in which METTL3 methylates the *Kras* transcript and other transcripts involved in growth factor signal transduction. Methylation promotes translation of these transcripts, maintaining responsiveness to extracellular growth factors and thus maintaining proliferation and survival in the transit amplifying cells of the crypt. TA cells make up most of the crypt and TA cell proliferation sustains the production of the absorptive enterocytes of the villus. Therefore, TA cell death reduces crypt and villus size and diminishes absorptive cell numbers without substantially impacting secretory cells, which are less dependent on transit amplification (4) (Figure 8).

We originally expected that METTL3 deletion would have no overt effect on the small intestinal epithelium because previous reports showed that METTL14 was dispensable in the small intestine (23, 24). Surprisingly, we found that small intestinal homeostasis requires METTL3. However, our study does not directly compare METTL3 and METTL14. Therefore, discrepancies between the present study and previously described METTL14 knockout studies could be due to facility-specific differences (e.g., microbiota). Several factors minimize this possibility. First, two independent groups from the US and China reported colonic but not small intestinal phenotypes with METTL14 knockout, demonstrating persistent phenotypes across mouse facilities. Furthermore, we found small intestinal phenotypes followed METTL3 deletion when testing both constitutive and inducible Cre-drivers, two *Mettl3-floxed* lines, microbiota-depleted mice, and mouse-derived enteroids. The consistency of small intestinal phenotypes spanning numerous orthogonal modes of METTL3 deletion strongly suggests that METTL3 and METTL14 act independently in the small intestine. This unexpected finding suggests divergent roles for METTL3 and METTL14 in the gut and underscores the value of examining m⁶A writer proteins in their native context.

Despite their critical role in maintaining homeostatic renewal of the intestinal epithelium, transit amplifying cell dynamics remain poorly understood. We propose that METTL3 is essential for both differentiation and renewal in the transit amplifying zone of the small intestinal crypt. As the site of stem progenitor differentiation, transit amplifying cells are critical to the process of lineage commitment in the cell (2). We observed general maintenance of secretory cells adjacent to areas of atrophic crypts in

Mettl3^{VilCre} and *Mettl3^{VilCreERΔ/Δ}* mice. In contrast, these histologically affected areas demonstrated little to no absorptive cell staining. Since mature absorptive cells make up most of the villus surface, transit amplification in the crypt is essential for the production of adequate numbers of absorptive progenitors rather than secretory cells (50). Consistent with our data showing decreased enterocyte maturation concurrent with loss of transit amplifying cells, a recent study suggested a causal relationship between decreased TA proliferation and an increase in the ratio of secretory to absorptive cells (4). Therefore, we propose that METTL3 promotes the production of absorptive cells by maintaining TA cell proliferation.

Inducible METTL3 deletion was also associated with extensive cell senescence and a >20-fold increase in the rate of cell death in the small intestinal crypt, especially in cells of the TA zone. TA cell death occurred only two days after deletion of METTL3, exceeded rates of cell death in the crypt base threefold, and occurred at a timepoint when markers of crypt base stem cells (*e.g.*, *Lgr5*) were preserved or even increased. Therefore, we conclude that METTL3 deletion causes an independent defect in transit amplifying cells. In a very recent publication, Liu et al. describe loss of LGR5+ intestinal epithelial stem cells three days after METTL3 deletion; they attribute loss of these stem cells to loss of pro-stemness transcription factors regulated by METTL3 (25). It is possible that defects in crypt base stem cells drives TA cell death rather than an intrinsic defect in TA cells, and we do not deny the possibility that crypt base stem cells require METTL3. However, we note that Liu et al. also observed extensive TUNEL staining in METTL3-depleted TA cells two days before they found a reduction in crypt base stem cells, corroborating our findings of primary TA cell death. Furthermore, a recent study posited that TA cells regulate the proliferation of LGR5+ stem cells by controlling the secretion of R-spondins (51). Thus, an initial defect in the TA zone could also precipitate the loss of LGR5+ crypt base stem cells. We therefore view the work of Liu et al. as both complementary to, and supporting of, our own findings. Our data, with the support of Liu et al., suggest that METTL3 specifically regulates the survival of intestinal transit amplifying cells.

Rapid proliferation in the TA zone suggests enhanced dependence on mitogenic factors in these cells. Consistent with this hypothesis, METTL3 deletion downregulated translation of multiple methylated transcripts involved in growth factor signaling, including: growth factor receptor *Fgfr4* (52), src family kinase *Yes1* (45), guanine nucleotide exchange factor *Tiam1* (53), and *Kras*. KRAS is a target of particular interest due to its role as an oncogene in the gut (43), where up to 50% of colorectal cancers

harbor a KRAS mutation (54). KRAS binds to guanosine 5'-triphosphate (GTP) in response to extracellular signals such as epidermal growth factor receptor (EGFR) activation. Activated KRAS-GTP then upregulates growth factor targets such as PI3K-Akt, RAF-MEK-ERK, and the GLUT1 glucose transporter (43). Although frequently dysregulated in cancer, these pathways are also essential for homeostatic proliferation, differentiation, and survival (55). Our data support a direct relationship between METTL3, *Kras* m⁶A-methylation, and KRAS protein levels. We posit that widescale depletion of growth factor signaling—including but not limited to KRAS—overwhelms cells of the TA zone and leads to cell death with METTL3 deletion.

In summary, we identify METTL3 as an essential post-transcriptional regulator of growth factor signaling and cell survival in transit amplifying cells, a critical but understudied cell type. This paves the way for future investigation of therapeutic targets that support transit amplifying cell resilience and function, including in the setting of DNA damaging agents such as chemotherapeutics and irradiation.

Methods

Animals

Mettl3^{VilCreΔ/Δ} and *Mettl3^{VilCreERΔ/Δ}* were generated by crossing *Vil-Cre 1000* mice (JAX #021504) or *Villin-CreERT2* mice (JAX #020282) to previously described *Mettl3^{flox/flox}* mice (32) kindly provided by Dr. Richard Flavell (Yale, New Haven, CT). *Mettl3^{VilCreERΔ2/Δ2}* were generated by crossing *Villin-CreERT2* mice to previously described *Mettl3^{flox2/flox2}* mice (33), kindly provided by Dr. Federica Accornero (Ohio State, Columbus, OH). For the m⁶A-seq experiment, wildtype mice were used (JAX #000664). All mice were C57BL/6J strain and both male and female mice were used. Mice were housed in a temperature-controlled room with 12-hour light and dark cycles and continuous access to food and water.

Tamoxifen injection, euthanasia criteria, and survival curves

Mice aged 8-9 weeks were injected four times with 50 mg/kg tamoxifen at 10 mg/mL in corn oil at 24-hour intervals. Mice were euthanized once they had reached humane endpoints defined by the IACUC protocol, including: >20% body weight loss, hunched posture, emaciated body condition, or non-responsiveness to stimuli. Survival curves were determined by the number of mice reaching a humane

endpoint on each day after tamoxifen injection. To assay inflammatory phenotype, mice spleen, intestines, and serum cytokines were measured in mice euthanized nine days post final tamoxifen injection, when all mice displayed daily reductions in weight and reached or approached critical body weight loss.

Microbial depletion

Mettl3^{flox/flox} and *Mettl3^{VilCreERΔ/Δ}* mice were moved to new cages at 7 weeks of age and given sterile DI water supplemented with 0.5g/L Ampicillin (Sigma A9518), 0.5g/L Neomycin (MP Biomedicals 180610), 0.5g/L Gentamicin (Sigma G1914-5G), 0.25g/L Vancomycin (VWR 0990), 0.25g/L Metronidazole (Thermo 210340050), and 4g/L Splenda to enhance taste. After seven days, mice were injected with tamoxifen for four days as described above and stool collected on the final day of injection. Stool from *Mettl3^{flox/flox}* and *Mettl3^{VilCreERΔ/Δ}* mice on normal drinking water was used as controls. DNA was extracted from stool using the QIAamp Fast DNA Stool Mini Kit (Qiagen 51604) and quantitative PCR was performed as described in the qPCR methods section using primer Ba04230899_s1. qPCR quantification was normalized to stool weight.

Serum cytokine quantification

Serum supernatant was isolated from the inferior vena cava of euthanized mice and cytokines measured using the Cytometric Bead Array (BD Biosciences) with the amount of capture beads, detection reagents, and sample volumes scaled down tenfold from manufacturer's protocol. Data was collected on an LSRFortessa flow cytometer (BD Biosciences) with FACSDiva v9.0 (BD Biosciences) and analyzed with FlowJo v10 (BD Biosciences). Statistical outliers were removed in GraphPad Prism v9.3 using ROUT method (Q=1%). Cytokines used were mouse TNFα (BD 558299), mouse IL-6 (BD 558301), mouse IL-1α (BD 560157), mouse IL-1β (BD 560232), mouse IL-10 (BD 558300), mouse IL-12/IL-23p40 (BD 560151), and mouse IFN-γ (BD 558296) with Mouse/Rat Soluble Protein Master Buffer Kit (BD 558266).

Histology and immunofluorescent staining

Intestines were Swiss-rolled and fixed overnight in 4% paraformaldehyde at 4°C prior to processing and embedding. Sections were blocked with Blocking Buffer (1% BSA and 10% donkey serum in PBS) for 1 hour, 25°C, before staining with primary antibodies (Supplemental Table 1) at 1:200 overnight at 4°C followed by washing with PBS and staining with secondary antibodies at 25°C for 25 minutes. Finally, nuclei were counterstained with 1:10,000 DAPI and coverslips mounted with Prolong® Gold Antifade Reagent. Duodenum, jejunum, and ileum were defined as the proximal, middle, and distal third of the small intestine. Proximal colon was defined as the proximal 4cm of the large intestine, and distal colon as the distal 4cm. For alkaline phosphatase staining, we used the Vector® Red Substrate Kit, Alkaline Phosphatase (Vector Laboratories SK-5100) on deparaffinized slides as described in the manufacturer's protocol. TUNEL was detected using the Click-iT™ Plus TUNEL Assay for In Situ Apoptosis Detection, Alexa Fluor™ 594 dye (Thermo C10618). For the β-Galactosidase staining, fresh frozen sections were stained overnight with the Senescence β Galactosidase Staining Kit (Cell Signaling 9860) per the manufacturer's protocol. All stains were imaged on the Keyence BZ-X100.

Histopathology and appearance scoring

Histopathological scoring was performed by blinded anatomical pathologist Dr. Benjamin Wilkins based on previously published criteria with an additional score for villus damage for small intestine (Supplemental Table 2) (56). For each category, the recorded score reflects the most severe finding. For percent involvement, the recorded score reflects the length of bowel that was involved by any of the scored processes. Scores were summed for each mouse to generate a separate composite score for small intestine and colon. Mouse appearance/behavior was scored according to a previously described rubric (57).

Intestinal epithelial organoid cultures

Intestinal sections were splayed open, rinsed in PBS, and rotated at 4°C for 45 minutes in Hank's Buffered Saline Solution with 10 mM EDTA and 1 mM N-Acetyl-L-cysteine (Sigma A9165). Crypts were isolated by scraping with a glass coverslip followed by vortexing and filtering through a 70 μm (small intestine) or 100 μm (colon) cell strainer. Crypt-enriched suspensions were centrifuged at 500xG, 25°C

for 5 minutes, washed in PBS, and pelleted again at 500xG, 25°C for 5 minutes. Crypts were plated in Matrigel droplets (Corning 354234) and unless stated otherwise, overlaid with the following “ENR” medium: advanced DMEM/F12 media (Thermo 12634028) containing 1X GlutaMAX (Thermo 35050061), 10 mM HEPES (Thermo 15-630-080), 1X Antibiotic Antimycotic (Thermo 15240062), 1X N-2 Supplement (Thermo 17502048), 1X B-27 Supplement (Thermo 17504044), 5 µM CHIR99021 (Cayman 13122), 1 mM N-Acetyl-L-cysteine (Sigma A9165), 50 ng/mL mEGF (PeproTech 315-09), 5% Noggin/R-spondin conditioned medium (generated using protocol from (34)), and 10 µM Y-27632 (LC Labs Y-5301). Colonic epithelial cultures were fed 50% WRN CM media (58). Passage-matched enteroids/colonoids were used for all experiments. For induction of CreERT2, enteroids/colonoids were given 1 µM 4-OHT in 100% ethanol at 48 and 24 hours before the start of the time course then mechanically passaged at day 0.

Whole mount staining in enteroids

Enteroids were dissociated to single cells using Accutase (STEMCELL Technologies 07920), resuspended in ENR supplemented with 10 µM Y-27632, and plated on chamber slides pretreated with 10% Matrigel in Advanced DMEM/F12. The next day, slides were incubated in 4% PFA at room temperature for 20 minutes and blocked in 10% goat serum in PBS for 30 minutes at 25°C. 1:200 rabbit monoclonal anti-METTL3 (abcam ab195352) and 1:200 goat polyclonal anti-E-Cadherin (R&D Systems AF748) were used at 37°C for 30 minutes, followed by 1:600 Alexa Fluor 488 AffiniPure Bovine Anti-goat IgG (Jackson 805-545-180) and Cy3 AffiniPure Donkey Anti-Rabbit IgG (Jackson 711-165-152) in PBS supplemented with 1:5000 DAPI. Chambers were detached from the chamber slide and coverslips mounted with Prolong® Gold Antifade Reagent. For the β-galactosidase staining, enteroids were grown embedded in Matrigel thinly smeared on standard tissue culture plates and stained overnight with the Senescence β Galactosidase Staining Kit (Cell Signaling 9860) per the manufacturer’s protocol. All stains were imaged on the Keyence BZ-X100.

qRT-PCR

RNA was isolated using the Quick-RNA Miniprep Kit (Zymo R1054). RNA was reverse transcribed using MultiScribe™ Reverse Transcriptase (Thermo 4311235) with random hexamer primers. Quantitative PCR

was performed using the Applied Biosystems TaqMan Fast Advanced Master Mix (Thermo 4444556) with TaqMan™ Gene Expression Assay (FAM) primers (Supplemental Table 3) on an Applied Biosystems QuantStudio 3.

Western blotting

Cells were lysed using RIPA buffer (Cell Signaling 9806S) supplemented with 1:100 protease phosphatase inhibitor (Cell Signaling 5872S) and protein concentration was measured using the Pierce™ BCA Protein Assay Kit (Thermo 23225). Lysates were boiled for 5 minutes with 100 mM DTT and 1X LDS buffer (GenScript M00676) and run on NuPAGE 4-12% Bis-Tris gels (Thermo NP0335BOX) in 1X MOPS-SDS buffer (BioWorld 10530007-2) or 1X MES-SDS buffer (Thermo NP0002, use for low MW proteins). Gels were transferred onto PVDF transfer membrane in 2X NuPAGE transfer buffer (Thermo NP006) and membranes blocked for 1 hr in 5% milk in TBS-T (TBS, 0.1% Tween-20), and then placed in 1:1000 primary antibody (Supplementary Table 1) overnight in 5% milk in TBS-T at 4°C. Blots were washed in TBS-T and placed in 1:2000 secondary antibody (Supplementary Table 1) for 1-2 hours at 25°C. Blots were then subjected to Supersignal® West Femto Maximum Sensitivity Chemiluminescent Substrate and imaged on the Biorad Gel Doc XR.

m⁶A dot blot

mRNA was isolated using the Dynabeads™ mRNA DIRECT™ Purification Kit (Thermo 61011). >30 ng of mRNA was heated to 65°C for 2 minutes, placed on ice for >5 minutes, and then pipetted onto a Hybond N+ nitrocellulose membrane and exposed to 254 nm UV light for 5 minutes. The nitrocellulose membrane was then washed in TBS-T (TBS, 0.1% Tween-20). Blots were then incubated in primary and secondary antibody and developed as described in the section on Western blotting. We detected m⁶A using anti-m⁶A primary antibody (Cell Signaling 56593). Total blotted mRNA was stained using 0.04% Methylene Blue (LabChem LC168508) in 0.5M sodium acetate.

RNA-seq and Polysome-seq

560 Ileal enteroids were expanded in Matrigel in 50% WRN media until 8 to 10 million cells per replicate was
561 achieved. Passage separated replicates from the same enteroid line were used. Media was
562 supplemented with 2 μ M 4-OHT 72 hours prior to collection. Enteroids were collected by mechanical
563 dissociation, pelleted, and snap frozen in liquid nitrogen. Frozen enteroid pellets were resuspended in ice-
564 cold lysis buffer containing 20mM Tris-HCl pH 7.4, 150mM MgCl₂, 150mM NaCl, 100 μ g/ml
565 cycloheximide, 1% v/v Triton X-100, 1mM DTT, 1U/ μ l SUPERase[•]IN RNase inhibitor (Thermo), 25U/ml
566 Turbo DNase1 (Thermo), and 1X EDTA-free protease inhibitor cocktail (Roche). Cells were lysed by
567 trituration through a 26-gauge needle 10 times. Samples were processed and libraries prepared as
568 previously described (41) with the following modifications. First, we performed sucrose cushion to pellet
569 the ribosome-associated mRNAs and proceeded with RNase I digestion (10 U/ μ l by the Epicentre
570 definition) for 30 μ g of RNA. Samples were incubated at room temperature for 45 minutes with gentle
571 agitation, and the digestion was quenched by adding 200 units of SUPERase[•]IN. Then, we directly
572 extracted the ribosome-protected fragments (RPF) using the TRIzol reagent and performed gel size
573 selection of the RPFs of 15-35 nucleotides in length. Second, we performed rRNA depletion using
574 RiboCop for Human/Mouse/Rat kit (Lexogen). Once the rRNA-depleted RPF fragments were obtained,
575 they were pooled together, and the libraries prepared with Unique molecular identifiers (UMIs) for
576 deduplication. The multiplexed library was then sequenced on Illumina HiSeq 4000 with PE150 runs
577 (paired end reading of 150 bases), with a sequencing depth of 60 million raw reads/sample. For each
578 sample, one-tenth (150 μ l) of the lysate was saved for RNA-seq. For RNA-seq, total RNA was extracted
579 using TRIzol LS reagent (Ambion) and purified using Quick-RNA Microprep kit (Zymo) following the
580 manufacturer's protocol. Libraries were prepared from total RNA using the Smarter[®] Stranded Total
581 RNA-Seq Kit v2 - Pico Input Mammalian (Takara Bio 634411) and sequenced on a Novaseq 6000, SP
582 Reagent Kit 1.5 (100 cycles). Raw sequencing data were demultiplexed, adaptors were removed using
583 cutadapt (59), contaminant sequences (rRNA and tRNA) were depleted, and reads were deduplicated
584 (umi_tools dedup). Reads were aligned to all transcripts on the mouse reference chromosomes (Gencode
585 version M31, GRCm39) using Kallisto (60). Analysis of ribosome-bound transcripts revealed many
586 transcripts smaller than the expected 29 nt ribosome footprint size (Supplemental Figure 6D). Since we
587 had sequenced RNAs from the polysome fraction of the sucrose cushion, but the RPF size did not meet

expectations, these data were only used for analysis of transcript-level information (translational efficiency), rather than codon level information. Translation efficiency (TE) was calculated by dividing the TPM in the total RNA library by the TPM in the ribosome-bound library for each individual transcript and sample. Differential gene expression for the RNA-seq was determined using DESeq2 (Bioconductor.org). Pathway enrichment analysis was performed using mouse gene symbols orthology-mapped to the human genome and tested against Gene Ontology Biological Process (GOBP) gene sets with the Molecular Signatures Database (gsea-msigdb.org).

m⁶A-seq

Three wildtype C57BL/6J mice (Jax #000664, 2 male 1 female) aged 8 weeks were used. Crypts were isolated from the distal half of the small intestine as described above and dissociated in 10% FBS in 1X PBS supplemented with 20 µg/mL Liberase TH (Roche 05401135001), and 35 µg/ml DNaseI (Roche 10104159001) for 20 minutes at 37°C with frequent agitation. Cell suspensions were then stained with 1:200 PE-EpCAM (BioLegend 118205), 1:200 FITC-CD45 (BioLegend 103107), and 1:1000 DRAQ7 (Thermo D15106) on ice for 30 minutes in the dark. ~800K live epithelial cells per mouse were then isolated by flow cytometry by sorting for DRAQ7- CD45- PE+ cells directly into Trizol LS (Ambion 10-296-010) on a FACSJazz Sorter. RNA was isolated from Trizol LS using the Direct-zol RNA Microprep Kit (Zymo R2062). RIP-seq was performed according to the “Refined RIP-seq” protocol for low input material (42) with the following specifications: 2 µg anti-m⁶A antibody (Synaptic Systems 202 003) was conjugated to magnetic beads and incubated with 6 µg total RNA that was previously fragmented to ~300 nt fragments with 10 mM ZnCl₂ in 10 mM Tris-HCl for 4 minutes at 70°C (5% of fragmented RNA was set aside as input). After 2 hours immunoprecipitation at 4°C, RNA-bead complexes were washed in high and low salt buffer and RNA was eluted from the RNA-bead complexes using the Qiagen RNeasy Plus Micro Kit (Qiagen 74034). Isolated m⁶A-enriched RNA was immunoprecipitated a second time using 2 µg of a second anti-m⁶A antibody (Abcam ab151230). Final cDNA Libraries were prepared from twice immunoprecipitated RNA and fragmented input total RNA using the Smarter® Stranded Total RNA-Seq Kit v2 - Pico Input Mammalian (Takara Bio 634411) and sequenced on a Novaseq 6000, SP Reagent Kit 1.5 (100 cycles). Raw reads were aligned to mm10 (gencode_M23_GRCm38.p6) using STAR aligner

(2.7.9a). N6-methyladenosine peaks were identified using exomePeak2 (version 1.2.0), followed by a metagene analysis using the bioconductor packages Guitar_2.10.0 and TxDb.Mmusculus.UCSC.mm10.knownGene_3.10.0.

m⁶A-RIP-qPCR

For m⁶A-RIP-qPCR, four *Mettl3*^{flox/flox} and four *Mettl3*^{VilCreERΔ/Δ} mice aged 8 weeks were used (2 male, 2 female mice per genotype). Intestinal crypts were isolated from the distal half of the small intestine as described above but without digestion to single cells. Whole crypts were pelleted, resuspended in TRI Reagent (Sigma 93289), and RNA was isolated using the Direct-zol RNA Miniprep Kit (Zymo R2050). Next, 20 μg of total RNA was fragmented and immunoprecipitated twice according to the “Refined RIP-seq protocol” as described above. Immunoprecipitated RNA and fragmented input total RNA was reverse transcribed using the High-Capacity cDNA Reverse Transcription Kit (Thermo 4368814) and qPCR was performed as described in the “qRT-PCR” section. For calculation of m⁶A enrichment, first we calculated the %input for every target in every RIP sample as $2^{-(\text{Ct of target gene in RIP} - \text{Ct of target gene in input sample})}$. Then we calculated m⁶A enrichment relative to *Gapdh* by dividing the %input of the target of interest (e.g., *Kras* 5' or 3'UTR) by the %input of *Gapdh* for each sample.

Lentiviral constructs and transduction

Accutase-digested (STEMCELL Technologies 07920) enteroids were resuspended in ENR with 1:4 lentivirus solution, TransDux MAX Lentivirus Transduction Enhancer (System Biosciences LV860A-1), and 10 uM Y-27632 and plated as monolayers on Collagen I (Advanced Biomatrix 5010). Lentiviral constructs and prepared virus were generated by VectorBuilder. The transfer vector for catalytic inactive METTL3 expression contained a CMV-EGFP:T2A:Puro selection cassette and the mPGK promoter upstream of the *Mus musculus Mettl3* ORF edited at ORF positions 1183-1194 from GACCCACCTTGG to GCCCACCTGCG yielding DPPW -> APPA synonymous mutation in the catalytic site as previously described (35). The transfer vector for KRAS or KRAS^{G12D} expression contained a CMV-EGFP:T2A:Puro selection cassette and the CMV promoter upstream of the *Mus musculus Kras* ORF either unedited (KRAS OE) or edited at ORF position 35 from G to A yielding G -> D synonymous mutation in the

regulatory site as previously described (KRAS^{G12D} OE) (61). The “GFP” control vector contained a CMV-mCherry:T2A:Puro selection cassette and the EGFP ORF under control of the CMV promoter. After overnight incubation with lentivirus, enteroid monolayers were mechanically dissociated and replated as 3D enteroids in Matrigel and selected for antibiotic resistance genes after 48 hours. The transfer vector expression rates (post-antibiotic selection) for all transgenic lines were determined by assessing rates of GFP reporter expression using flow cytometry and are given in Supplementary Table 4.

Quantification and statistical analysis

Unless otherwise noted, quantification of immunofluorescent staining was performed using three representative images taken per mouse using a 20X objective. Images were taken in three areas of most severe histological distortion (defined as a high-powered field with greatest changes in crypt and/or villus morphology) in distal half of the small intestine of tested mice. Three representative sections were chosen from matching regions of the distal half of the small intestine in control mice. Quantification was performed by individuals blinded to mouse genotype. Unless otherwise noted, each graphed data point is the mean of three quantified representative images per mouse. P values were calculated with the unpaired parametric Student's t test in GraphPad Prism. P values for survival curves were calculated using the Log-rank Mantel-Cox test in GraphPad Prism. Unless otherwise noted, p values <0.05 were considered significant.

Study approval

Mouse experiments and handling were approved under IACUC protocol 001278 at the Children's Hospital of Philadelphia.

Data and materials availability:

All data needed to evaluate the conclusions in the paper are present in the paper and/or the Supplementary Materials. Values for all data points in graphs are reported in the Supporting Data Values file. Raw sequencing data are uploaded to Dryad at <https://doi.org/10.5061/dryad.5tb2rbp8s>.

Author contributions:

Conceptualization: CHD, KEH

Methodology: CHD, EAM, SV, PS

Formal analysis: CHD, KEH², SV, YZ, BJW

Investigation: CHD, KEN, SV, RM, SKN, KK, LP, XM, AC

Visualization: CHD, KEH²

Supervision: CHD, KEH, PS, MDW

Writing—original draft: CHD, KEH

Writing—review & editing: CHD, KEH, MDW, KEN, KK

KEH: Kathryn E. Hamilton

KEH²: Katharina E. Hayer

Acknowledgments

We thank Dr. Richard Flavell (Yale University), Dr. Federica Accornero (Ohio State University), and Dr. Brian Capell (University of Pennsylvania Perelman School of Medicine) for generously providing Mettl3-floxed mice used in this study. For feedback, technical assistance, and/or sharing of laboratory reagents, we thank: Dr. Michael Silverman, Dr. Michael Abt, Dr. Tatiana Karakasheva, Gloria Soto, Dr. Amanda Muir, Dr. Masaru Sasaki, Joshua Wang, Dr. Lan Lin, Dr. Samir Adhikari, Dr. Derek Sung, and Nora Kiledjian (Children's Hospital of Philadelphia/University of Pennsylvania Perelman School of Medicine) and Dr. Igor Brodsky, Dr. Chris Lengner, and Zvi Cramer (University of Pennsylvania School of Veterinary Medicine). We also thank the following scientific cores and centers: The Center for Molecular Studies in Digestive and Liver Diseases (P30DK050306) and the Molecular Pathology and Imaging Core (RRID: SCR_022420), the Flow Cytometry Core at the Children's Hospital of Philadelphia, and the Center for Applied Genomics at the Children's Hospital of Philadelphia. Artwork depicting mouse injection schemes was created with BioRender.com

Funding:

NIDDK R01-DK124369 (KEH)

NIEHS R21-ES031533 (KEH)

The Children's Hospital of Philadelphia Institutional Development Funds (KEH)

The Gastrointestinal Epithelium Modeling Program (KEH)

References

1. Peterson LW, Artis D. Intestinal epithelial cells: Regulators of barrier function and immune homeostasis. *Nat. Rev. Immunol.* 2014;14(3):141–153.
2. Gehart H, Clevers H. Tales from the crypt: new insights into intestinal stem cells. *Nat. Rev. Gastroenterol. Hepatol.* 2019;16(1):19–34.
3. Yousefi M, et al. Hierarchy and Plasticity in the Intestinal Stem Cell Compartment. *Trends Cell Biol.* 2017;27(10):753–764.
4. Sanman LE, et al. Transit-Amplifying Cells Coordinate Changes in Intestinal Epithelial Cell-Type Composition. *Dev. Cell* 2021;56(3):356–365.e9.
5. Ding X, et al. Crypt Base Columnar Stem Cells in Small Intestines of Mice Are Radioresistant. *Gastroenterology* 2012;16(3):387–393.
6. Gibson RJ, et al. Irinotecan causes severe small intestinal damage, as well as colonic damage, in the rat with implanted breast cancer. *J. Gastroenterol. Hepatol.* 2003;18(9):1095–1100.
7. Sansom OJ, et al. MBD4 deficiency reduces the apoptotic response to DNA-damaging agents in the murine small intestine. *Oncogene* 2003;22(46):7130–7136.
8. Chen G, et al. Radiotherapy-Induced Digestive Injury: Diagnosis, Treatment and Mechanisms. *Front. Oncol.* 2021;11:757973.
9. Di Fiore F, Van Cutsem E. Acute and long-term gastrointestinal consequences of chemotherapy. *Best Pract. Res. Clin. Gastroenterol.* 2009;23(1):113–24.
10. Secombe KR, et al. The bidirectional interaction of the gut microbiome and the innate immune system: Implications for chemotherapy-induced gastrointestinal toxicity. *Int. J. Cancer* 2019;144(10):2365–2376.
11. Chatterji P, et al. Posttranscriptional regulation of colonic epithelial repair by RNA binding protein IMP1/IGF2BP1. *EMBO Rep.* 2019;20(6):1–16.
12. Chatterji P, et al. The LIN28B–IMP1 post-transcriptional regulon has opposing effects on oncogenic signaling in the intestine. *Genes Dev.* 2018;32(15–16):1020–1034.
13. Han B, et al. YTHDF1-mediated translation amplifies Wnt-driven intestinal stemness. *EMBO Rep.* 2020;1–14.
14. Jabs S, et al. Impact of the gut microbiota on the m6A epitranscriptome of mouse cecum and liver. *Nat. Commun.* 2020;11(1):1–16.
15. Olazagoitia-Garmendia A, et al. Gluten-induced RNA methylation changes regulate intestinal inflammation via allele-specific XPO1 translation in epithelial cells. *Gut* 2022;71(1):68–77.
16. Meyer KD, et al. Comprehensive analysis of mRNA methylation reveals enrichment in 3' UTRs and near stop codons. *Cell* 2012;149(7):1635–1646.
17. Dominissini D, et al. Topology of the human and mouse m6A RNA methylomes revealed by m6A-seq. *Nature* 2012;485(7397):201–206.
18. Murakami S, Jaffrey SR. Hidden codes in mRNA: Control of gene expression by m6A. *Mol. Cell* 2022;82(12):2236–2251.
19. Jabs S, et al. Impact of the gut microbiota on the m6A epitranscriptome of mouse cecum and liver. *Nat. Commun.* 2020;11(1). doi:10.1038/s41467-020-15126-x
20. Zhang J, et al. m6A modification in inflammatory bowel disease provides new insights into clinical applications. *Biomed. Pharmacother.* 2023;159:114298.
21. Wang P, et al. Structural Basis for Cooperative Function of Mettl3 and Mettl14 Methyltransferases. *Mol. Cell* 2016;63(2):306–317.
22. Wang X, et al. Structural basis of N6-adenosine methylation by the METTL3-METTL14 complex.

Nature 2016;534(7608):575–578.

23. Zhang T, et al. m6A mRNA modification maintains colonic epithelial cell homeostasis via NF- κ B-mediated antiapoptotic pathway. *Sci. Adv.* 2022;8(12). doi:10.1126/sciadv.abl5723

24. Du J, et al. N6-adenomethylation of GsdmC is essential for Lgr5+ stem cell survival to maintain normal colonic epithelial morphogenesis. *Dev. Cell*; doi:10.1016/j.devcel.2022.07.006

25. Liu Y, et al. Segregation of the stemness program from the proliferation program in intestinal stem cells. *Stem Cell Reports* 2023;18. doi:10.1016/j.stemcr.2023.03.007

26. Madison BB, et al. Cis Elements of the Villin Gene Control Expression in Restricted Domains of the Vertical (Crypt) and Horizontal (Duodenum, Cecum) Axes of the Intestine. *J. Biol. Chem.* 2002;277(36):33275–33283.

27. Wang A, et al. m6A modifications regulate intestinal immunity and rotavirus infection [Internet]. *Elife* 2022;11. doi:10.7554/eLife.73628

28. Zeng Z, et al. METTL3 protects METTL14 from STUB1-mediated degradation to maintain m6A homeostasis. *EMBO Rep.* 2023;24(3):e55762.

29. Wang Y, et al. N6-methyladenosine modification destabilizes developmental regulators in embryonic stem cells. *Nat. Cell Biol.* 2014;16(2):191–8.

30. Gustafsson JK, Johansson MEV. The role of goblet cells and mucus in intestinal homeostasis. *Nat. Rev. Gastroenterol. Hepatol.* 2022;19(12):785–803.

31. Wallaey C, et al. Paneth cells as the cornerstones of intestinal and organismal health: a primer. *EMBO Mol. Med.* 2022;1–26.

32. Li HB, et al. m6A mRNA methylation controls T cell homeostasis by targeting the IL-7/STAT5/SOCS pathways. *Nature* 2017;548(7667):338–342.

33. Shay G, et al. m6A mRNA methylation facilitates resolution of naïve pluripotency toward differentiation. *Science (80-)*. 2015;347(6225):1002–1006.

34. Sato T, et al. Single Lgr5 stem cells build crypt-villus structures in vitro without a mesenchymal niche. *Nature* 2009;459(7244):262–265.

35. Clancy MJ, et al. Induction of sporulation in *Saccharomyces cerevisiae* leads to the formation of N6-methyladenosine in mRNA: A potential mechanism for the activity of the IME4 gene. *Nucleic Acids Res.* 2002;30(20):4509–4518.

36. Lin S, et al. The m6A Methyltransferase METTL3 Promotes Translation in Human Cancer Cells. *Mol. Cell* 2016;62(3):335–345.

37. Choe J, et al. mRNA circularization by METTL3–eIF3h enhances translation and promotes oncogenesis. *Nature* 2018;561(7724):556–560.

38. Wei X, et al. METTL3 preferentially enhances non-m6A translation of epigenetic factors and promotes tumorigenesis. *Nat. Cell Biol.* 2022;24(8):1278–1290.

39. Zaccara S, Jaffrey SR. A Unified Model for the Function of YTHDF Proteins in Regulating m6A-Modified mRNA. *Cell* 2020;181(7):1582–1595.e18.

40. Meyer KD, et al. 5' UTR m6A Promotes Cap-Independent Translation. *Cell* 2015;163(4):999–1010.

41. Cope AL, et al. Exploring Ribosome-Positioning on Translating Transcripts with Ribosome Profiling. *Methods Mol. Biol.* 2022;2404:83–110.

42. Zeng Y, et al. Refined RIP-seq protocol for epitranscriptome analysis with low input materials. *PLoS Biol.* 2018;16(9):1–20.

43. Ternet C, Kiel C. Signaling pathways in intestinal homeostasis and colorectal cancer: KRAS at centre stage. *Cell Commun. Signal.* 2021;19(1):1–22.

44. Liu J, et al. Landscape and Regulation of m6A and m6Am Methylome across Human and Mouse Tissues. *Mol. Cell* 2020;77(2):426–440.e6.

45. Garmendia I, et al. YES1: A Novel Therapeutic Target and Biomarker in Cancer. *Mol. Cancer Ther.* 2022;21(9):1371–1380.

46. Niu X, et al. The nuclear pore complex function of sec13 protein is required for cell survival during retinal development. *J. Biol. Chem.* 2014;289(17):11971–11985.

47. Groen EJN, Gillingwater TH. UBA1: At the Crossroads of Ubiquitin Homeostasis and Neurodegeneration. *Trends Mol. Med.* 2015;21(10):622–632.

48. Alexander PB, et al. EGF promotes mammalian cell growth by suppressing cellular senescence. *Cell Res.* 2015;25(1):135–8.

49. Bohin N, et al. Genome Toxicity and Impaired Stem Cell Function after Conditional Activation of CreER T2 in the Intestine. *Stem Cell Reports* 2018;11(6):1337–1346.

50. Tóth B, et al. Early commitment and robust differentiation in colonic crypts. *Mol. Syst. Biol.* 2017;13(1):902.
51. Qu M, et al. Establishment of intestinal organoid cultures modeling injury-associated epithelial regeneration. *Cell Res.*; doi:10.1038/s41422-020-00453-x
52. Liu Y, et al. Dissecting the Role of the FGF19-FGFR4 Signaling Pathway in Cancer Development and Progression. *Front. Cell Dev. Biol.* 2020;8(February):1–9.
53. Boissier P, Huynh-Do U. The guanine nucleotide exchange factor Tiam1: A Janus-faced molecule in cellular signaling. *Cell. Signal.* 2014;26(3):483–491.
54. Peeters M, et al. Prevalence of RAS mutations and individual variation patterns among patients with metastatic colorectal cancer: A pooled analysis of randomised controlled trials. *Eur. J. Cancer* 2015;51(13):1704–13.
55. Johnson L, et al. K-ras is an essential gene in the mouse with partial functional overlap with N-ras. *Genes Dev.* 1997;11(19):2468–2481.
56. Dieleman LA, et al. Chronic experimental colitis induced by dextran sulphate sodium (DSS) is characterized by Th1 and Th2 cytokines. *Clin. Exp. Immunol.* 1998;114(3):385–91.
57. Paster EV, Villines KA, Hickman DL. Endpoints for mouse abdominal tumor models: refinement of current criteria. *Comp. Med.* 2009;59(3):234–41.
58. Miyoshi H, Stappenbeck TS. In vitro expansion and genetic modification of gastrointestinal stem cells in spheroid culture. *Nat. Protoc.* 2013;8(12):2471–2482.
59. Martin M. Cutadapt removes adapter sequences from high-throughput sequencing reads. *EMBnet.journal* 2011;17(1):10.
60. Bray NL, et al. Near-optimal probabilistic RNA-seq quantification. *Nat. Biotechnol.* 2016;34(5):525–527.
61. Valenzuela DM, Groffen J. Four human carcinoma cell lines with novel mutations in position 12 of c-K-ras oncogene. *Nucleic Acids Res.* 1986;14(2):843–52.

835 **Figures**
836

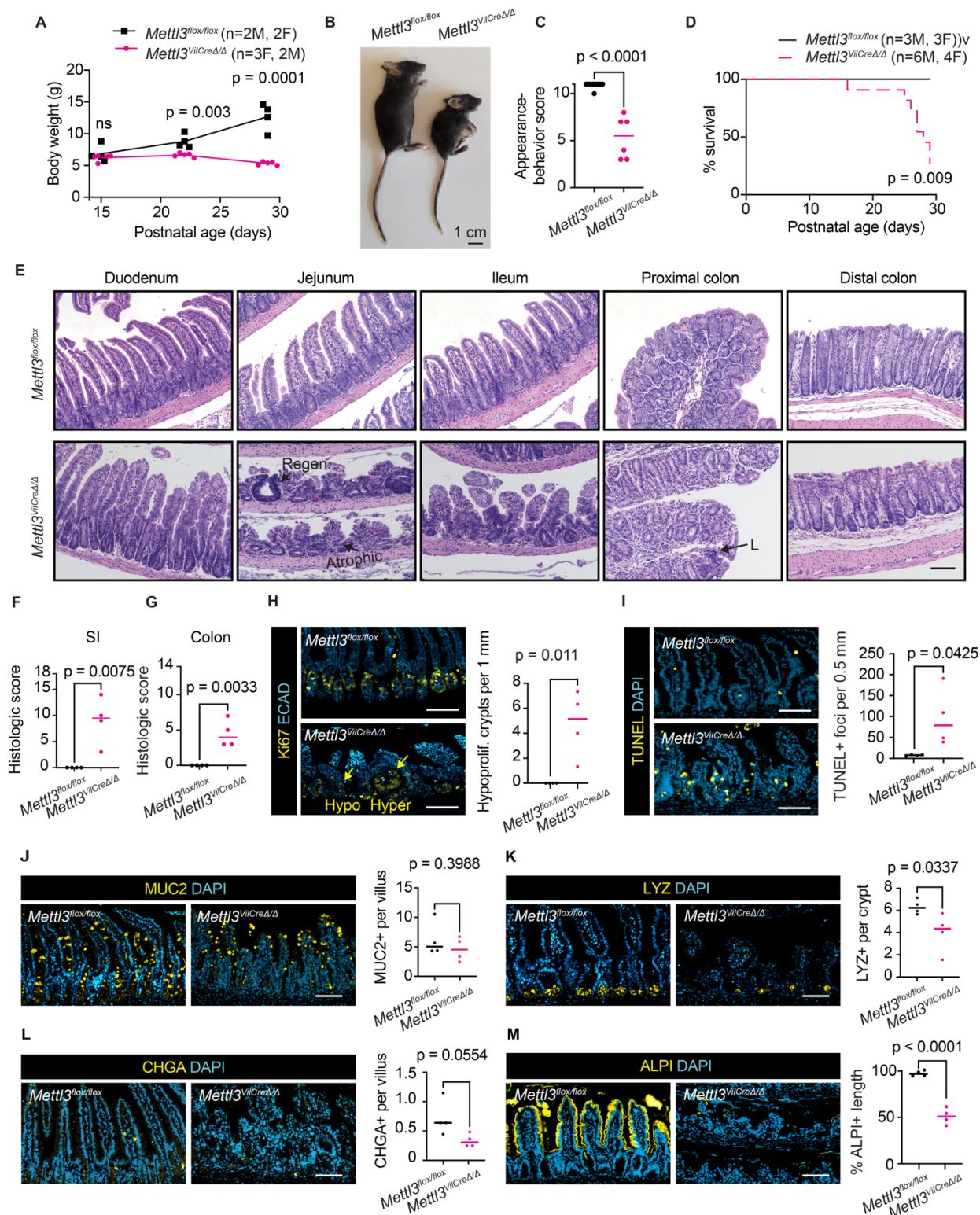


Figure 1. Constitutive METTL3 deletion causes growth retardation and small intestinal epithelial distortion. (A) Growth curves from postnatal day 15 to 29. (B) Gross appearance at postnatal day 29. (C) Composite appearance and behavior score at postnatal day 29. (D) Kaplan-Meier survival curves through

postnatal day 29; p value corresponds to Log-rank (Mantel-Cox) test. **(E)** Representative small intestine and colon H&E images. Regenerative and atrophic crypts are highlighted. "L" denotes lymphocytic infiltrate. **(F, G)** Composite histological score for small intestine (SI) and colon. **(H)** Representative images of Ki67 in distal small intestine and number of hypo-proliferative crypts (<10 Ki67+ cells) crypts per one mm distal half small intestine. Hypo- and hyper-proliferative crypts are highlighted. **(I)** Representative images and quantification of TUNEL staining **(J, K, L)** Representative images and quantification of intestinal secretory markers MUC2, LYZ, and CHGA **(M)** Representative images and quantification of percent alkaline phosphatase positive villus length. Each plotted point corresponds to one mouse and depicts the mean of three representative sections imaged per mouse with bar at median value. Unless otherwise noted, p value represents unpaired parametric Student's t test. Immunofluorescence staining and quantification performed in distal half small intestine. All scale bars 100 μ M.

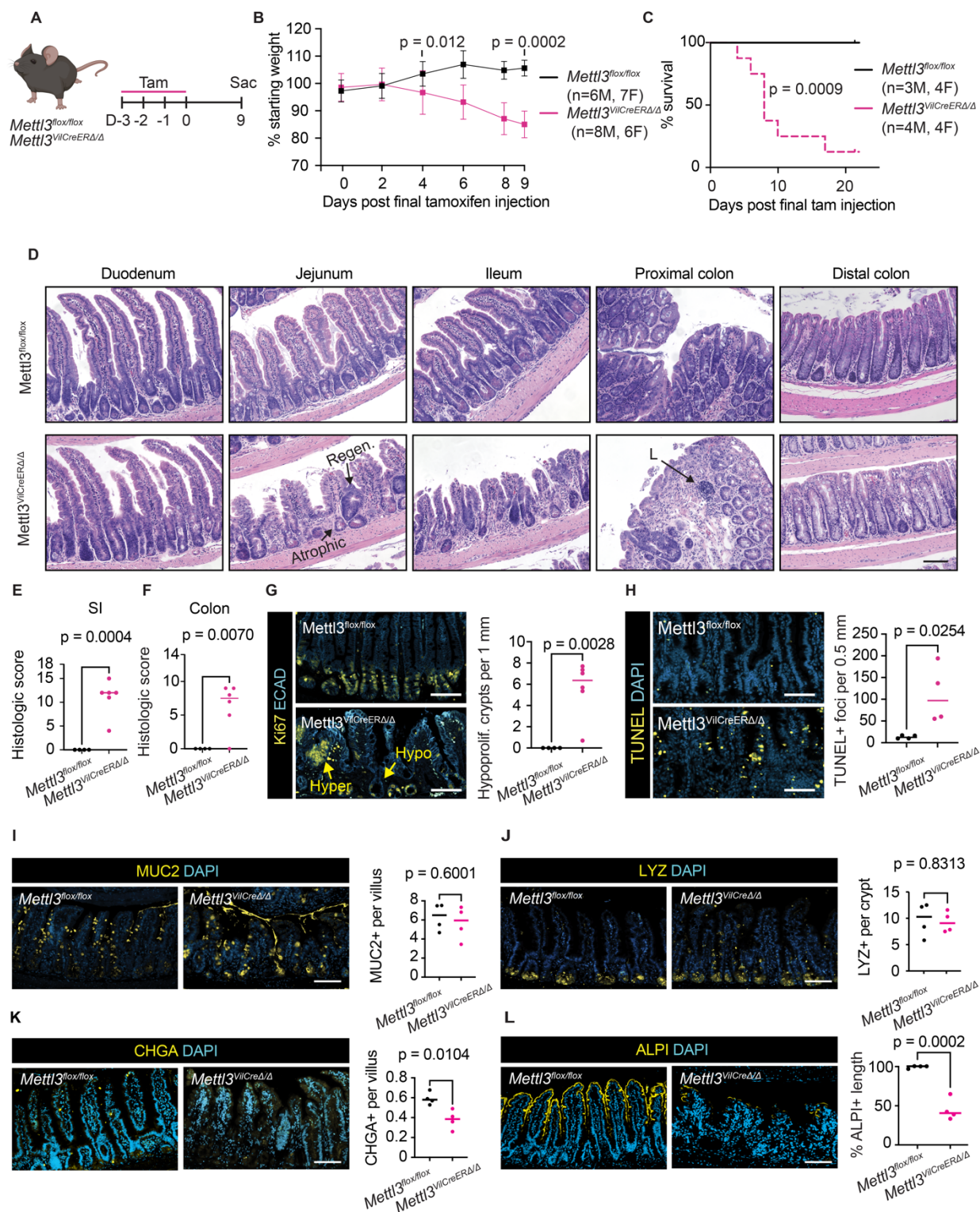


Figure 2. Inducible METTL3 deletion causes mortality and small intestinal epithelial disruption in adult mice. (A) Experimental schematic depicting sacrifice nine days post final tamoxifen injection. (B) Weight curves through nine days post tamoxifen injection, mean \pm SD. (C) Kaplan-Meier survival curves through 22 days post final tamoxifen injection, p value corresponds to Log-rank (Mantel-Cox) test. (D) Representative small intestine and colon H&E images. Regenerative and atrophic crypts are highlighted.

859 “L” indicates lymphocytic infiltrate. **(E, F)** Composite histological score for small intestine (SI) and colon. **(G)**
860 Representative images of Ki67 and quantification of hypo-proliferative (<10 Ki67+ cells) crypts per one mm
861 intestine. Hypo- and hyper-proliferative crypts are highlighted. **(H)** Representative images and quantification
862 of TUNEL staining. **(I, J, K)** Representative images and quantification of intestinal secretory markers MUC2,
863 LYZ, and CHGA. **(L)**. Representative images and quantification of percent alkaline phosphatase villus
864 length. Unless otherwise noted, each data point corresponds to one mouse and depicts the mean of three
865 representative sections imaged per mouse with bar at median value. Unless otherwise noted, p value
866 represents unpaired parametric Student's t test. Immunofluorescence staining and quantification performed
867 in distal half small intestine. All scale bars 100 μ M.

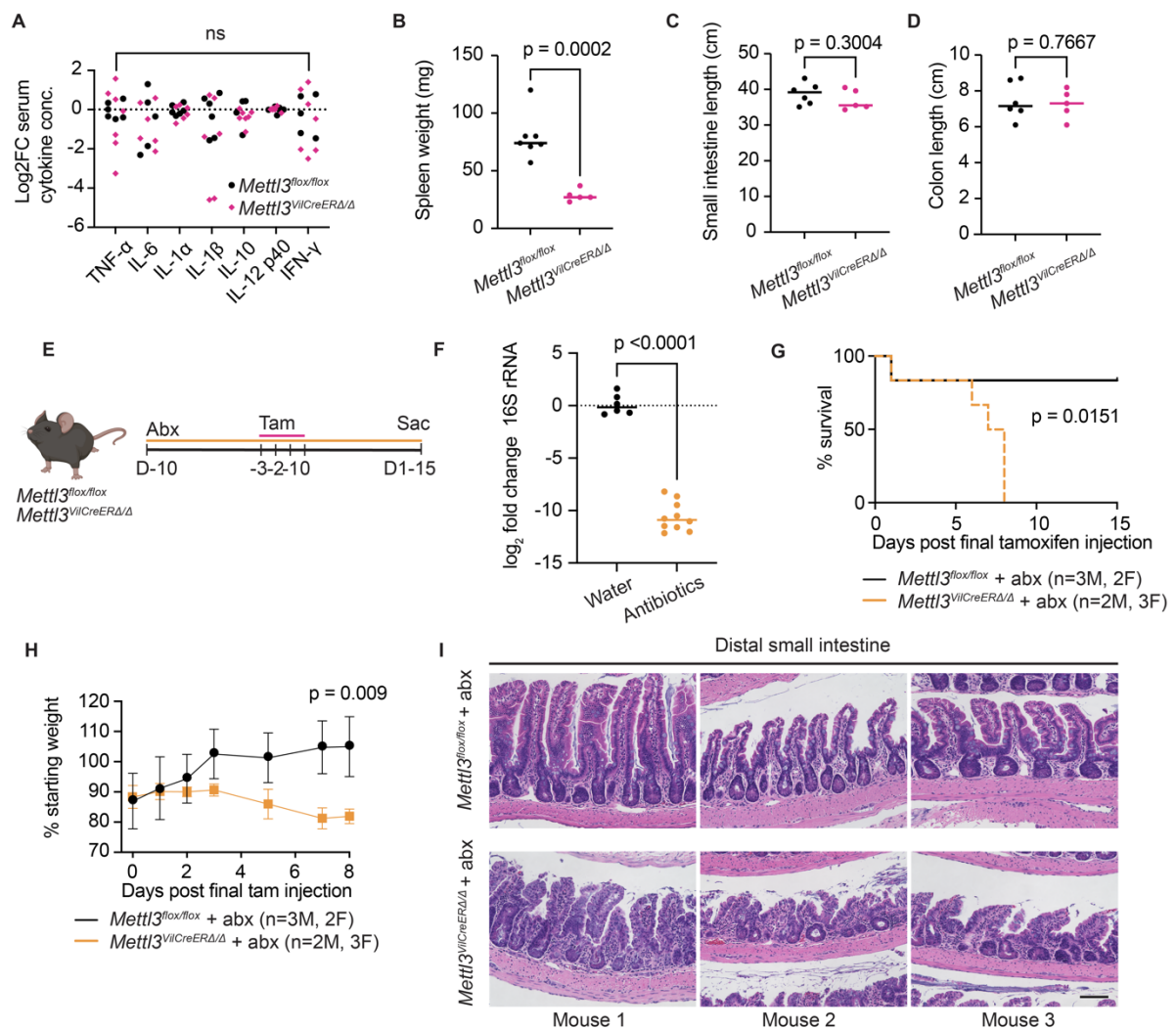


Figure 3. Intestinal distortion and mortality after METTL3 deletion is microbiota independent. (A) Log₂ fold change in serum cytokines in mice nine days post final tamoxifen injection, ns indicates $p > 0.05$ for the KO vs control comparison for each individual cytokine. Statistical outliers were removed in GraphPad Prism v9.3 using ROUT method ($Q=1\%$). **(B)** Spleen weight nine days post final tamoxifen injection. **(C, D)** Small intestine and colon length nine days post final tamoxifen injection. **(E)** Experimental schematic depicting timing of antibiotic (abx) treatment, tamoxifen injection, and sacrifice. **(F)** Log₂ fold change in 16S rRNA amplified from fecal bacterial DNA on final day of tamoxifen injection in antibiotic-treated or water vehicle mice. **(G)** Kaplan-Meier survival curves through 15 days post final tamoxifen injection in antibiotic treated mice, p value corresponds to Log-rank (Mantel-Cox) test. **(H)** Weight change post final tamoxifen injection in antibiotic treated mice, presented as mean \pm SD, p value represents unpaired parametric Student's t test for values at 8 days post final tamoxifen injection. **(I)** Representative H&E images from matched sections of distal small intestine in $n=3$ antibiotic treated mice per genotype. Unless otherwise noted, each data point represents a single mouse with bar at median value and p denotes value of unpaired parametric Student's t test. Scale bar 100 μ M.

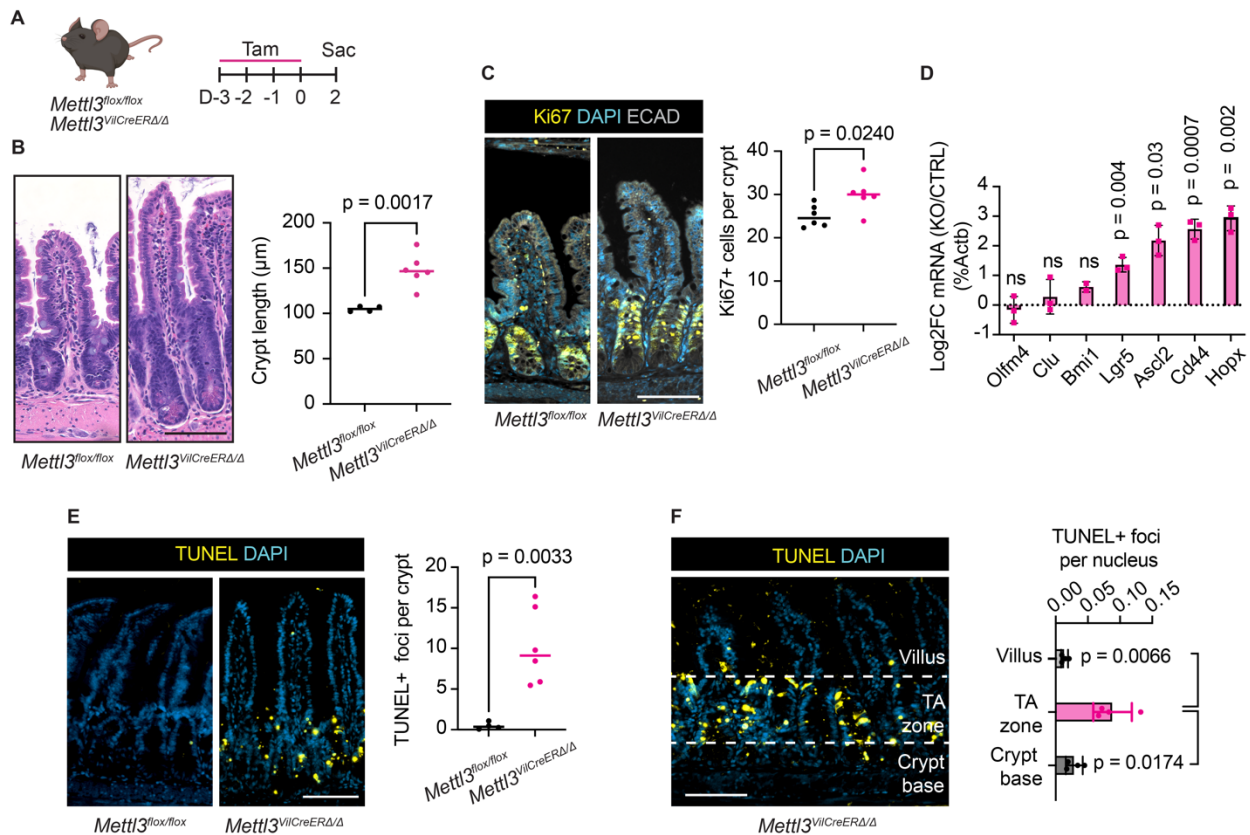


Figure 4. METTL3 deletion rapidly induces death of transit amplifying cells. (A) Experimental schematic depicting early sacrifice two days post tamoxifen injection. (B) Representative images and quantification of crypt height. (C) Representative images and quantification of Ki67 staining. (D) Log₂ fold change in qPCR quantification of indicated genes in *Mettl3*^{ViiCreERΔ/Δ} distal small intestinal crypts relative to the mean of *Mettl3*^{flox/flox} controls and normalized to *Actb*. Data presented as mean +/- SD. (E) Representative images and quantification of TUNEL staining (F) Representative image and quantification of distribution of TUNEL staining in villus, transit amplifying (TA) zone, and crypt base in *Mettl3*^{ViiCreERΔ/Δ} mice. Data presented as mean +/- SD. Each plotted data point corresponds to one mouse. For IF, each data point depicts the mean of three representative sections imaged per mouse with bar at median value. P value represents unpaired parametric Student's t test. All data from distal small intestine of mice two days post final tamoxifen injection. All scale bars 100 μm.

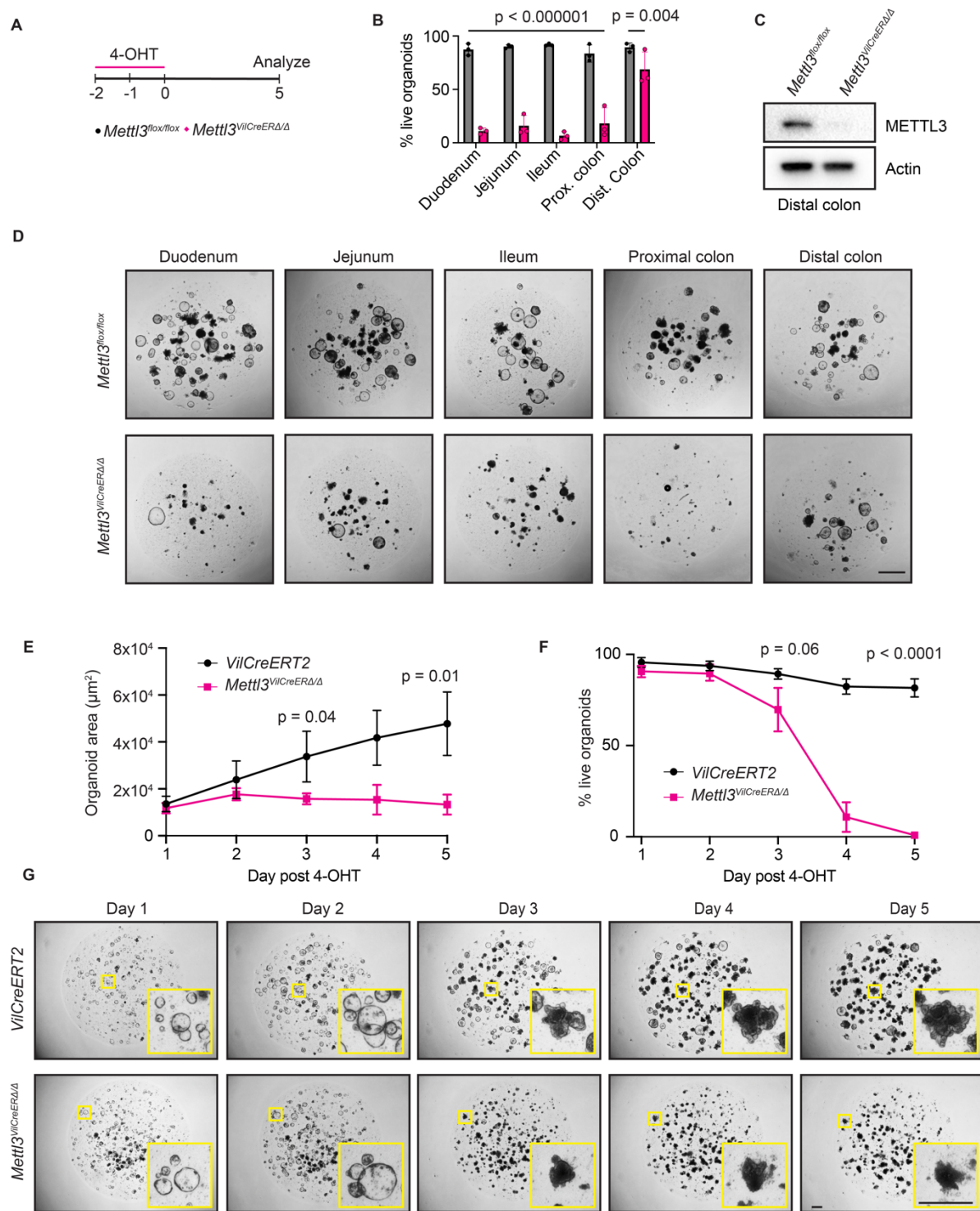


Figure 5. METTL3 deletion triggers growth arrest and death in intestinal epithelial enteroids and colonoids. (A) Intestinal epithelial enteroids or colonoids were treated with 1 μM 4-OHT 48 and 24 hours before beginning of time course and analyzed at days 1 through 5. (B) Percent live enteroids or colonoids from indicated tissue regions at five days post 4-OHT treatment. Each point represents $n=9$ technical replicates across $n=3$ passage separated biological replicates per genotype. Data presented as median \pm SD. P value represents unpaired parametric Student's t test. (C) Western blot for METTL3 in surviving distal colonoids six days after 4-OHT treatment. (D) Representative images at five days post 4-OHT treatment

corresponding to quantification in (B). Scale bar 500 μ M **(E, F)** ImageJ quantification of average enteroid 2D area and percent live enteroids in each of the five days post 4-OHT treatment of *Villin-CreERT2* (VilCreERT2) and *Mettl3^{VilCreERT2}* ileal enteroids. Each point represents n=9 technical replicates across n=3 passage separated biological replicates per genotype. Data presented as mean \pm SD. P value represents unpaired parametric Student's t test at day 3 and day 5. **(G)** Representative images of ileal enteroids in the five days post 4-OHT treatment. Scale bar 200 μ M.

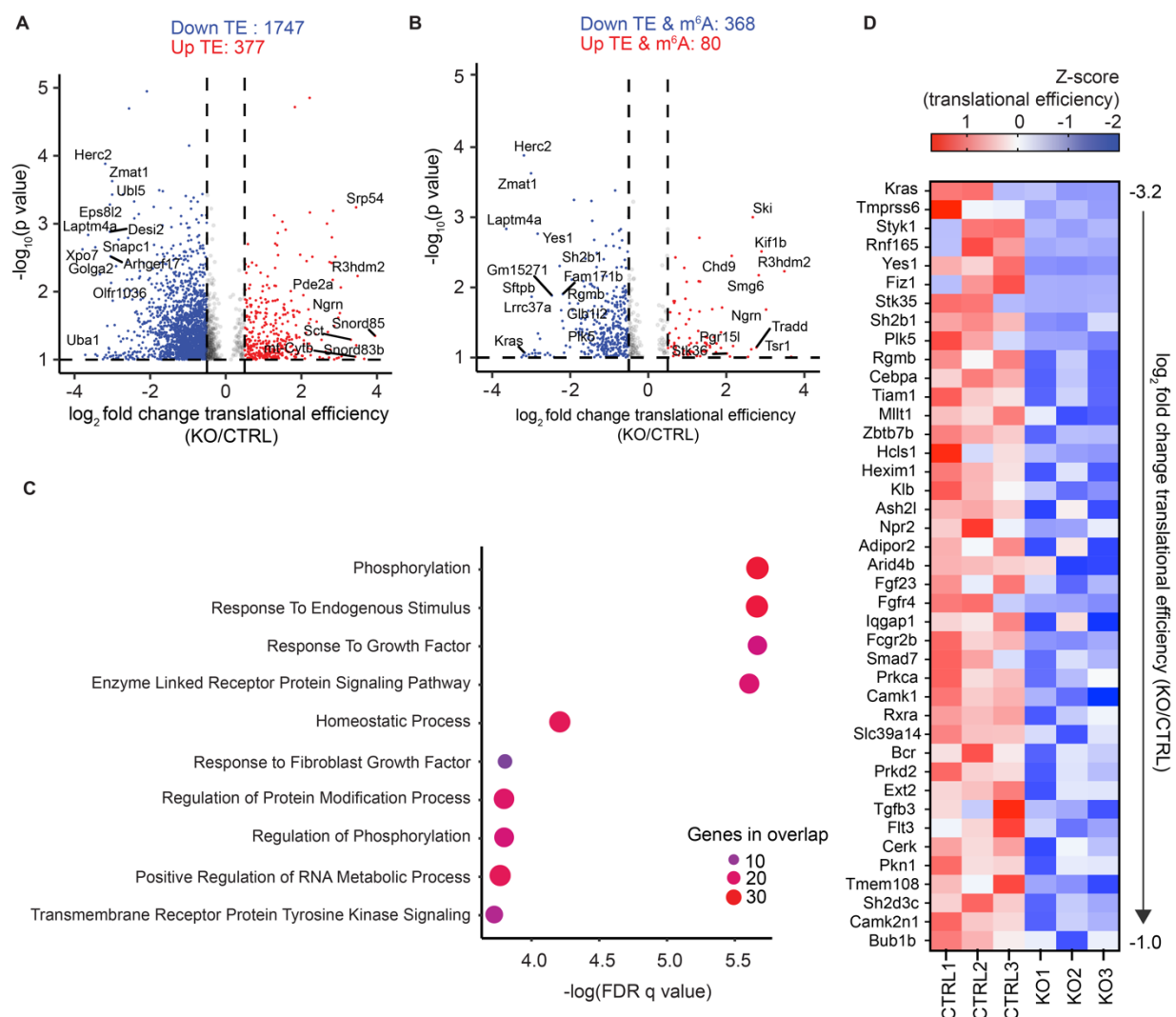


Figure 6. METTL3 deletion leads to a global decrease in mRNA translational efficiency with impacts on growth factor signaling. (A) Volcano plot of all transcripts with log₂ fold change in translational efficiency (TE) >0.5 or <-0.5 and -log₁₀ p value >1. Red marks all transcripts with increased TE and blue marks all transcripts with decreased TE. (B) Volcano plot of all transcripts displayed in (A), now filtered for transcripts containing at least one m⁶A peak. (C) Pathway enrichment analysis comparing transcripts with downregulated TE (log₂FC < -1) and at least one m⁶A peak against Gene Ontology Biological Process (GOBP) gene sets. Circle color and size both scale with number of genes overlapping between the tested gene set and the GOBP gene set. (D) Heat map depicting Z-scores for TE. Genes presented are all 42 unique genes from the four most significantly enriched pathways in (C). Genes are presented in order of greatest decrease in mean TE to smallest decrease. All data from RNA-seq and polysome-seq in n=3 *Mettl3*^{flox/flox} (CTRL) and n=3 *Mettl3*^{VilCreERΔ/Δ} (KO) ileal enteroids 72 hours post initiation of 4-OHT treatment.

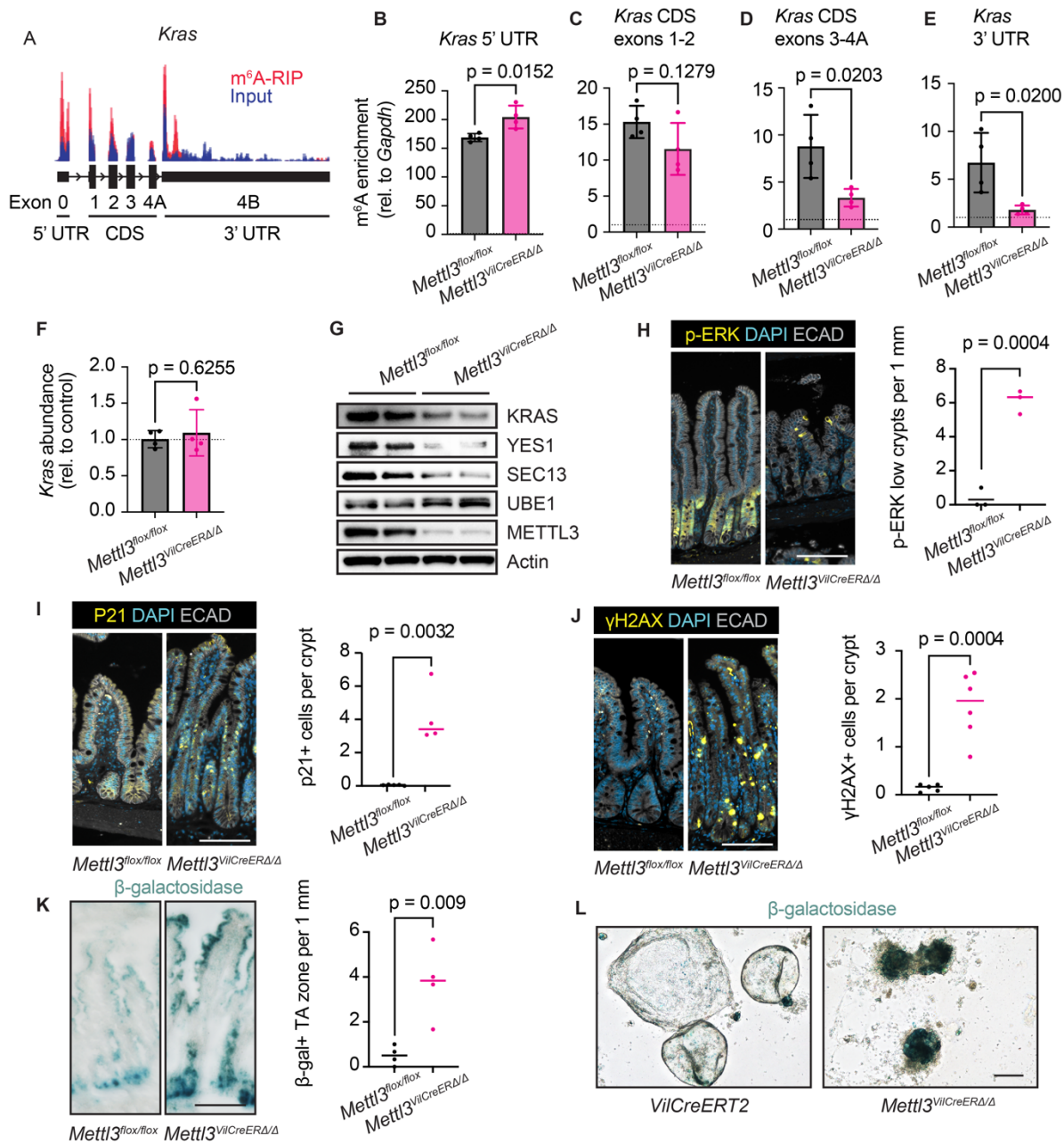


Figure 7. METTL3 deletion downregulates KRAS and induces cellular senescence. (A) Integrated Genomics Viewer depiction of read density for m⁶A-RIP (red) and input RNA (blue) for the *Kras* transcript as determined by m⁶A-seq in distal small intestinal crypts of n=3 wildtype mice. (B, C, D, E) m⁶A-enrichment determined by m⁶A-RIP-qPCR with primers targeting *Kras* 5' UTR, CDS Exons 1-2, CDS Exons 3-4A, and 3' UTR in crypt enriched lysates from *Mettl3*^{flx/flx} and *Mettl3*^{VilCreERΔ/Δ} mice three days post-tamoxifen. Data presented as mean +/- SD. Dotted line at m⁶A-enrichment = 1. (F) qPCR for *Kras* transcript in crypt enriched lysates from *Mettl3*^{flx/flx} and *Mettl3*^{VilCreERΔ/Δ} mice three days post-tamoxifen. Data normalized to *Actb* and the mean of *Mettl3*^{flx/flx} controls. Data presented as mean +/- SD. (G) Western blot for top targets with downregulated TE in crypts of *Mettl3*^{flx/flx} and *Mettl3*^{VilCreERΔ/Δ} mice two days post final tamoxifen injection (n=2 mice per genotype). (H) Representative images and quantification of phospho-ERK staining in atrophic small intestinal crypts in *Mettl3*^{VilCreERΔ/Δ} mice and region-matched *Mettl3*^{flx/flx} controls nine days post final

tamoxifen injection. “p-ERK low” crypts contain <5 p-ERK+ cells. **(I, J, K)** Representative images and quantification of p21, γ H2AX, and β -galactosidase staining in distal half small intestine of *Mettl3^{flox/flox}* and *Mettl3^{VilCreERT2}* mice two days post final tamoxifen injection. **(L)** β -galactosidase staining in control *VilCreERT2* and *Mettl3^{VilCreERT2}* enteroids three days post 4-OHT. For all plots, each data point represents a single mouse and p denotes value of unpaired parametric Student’s t test. Unless otherwise noted, immunofluorescence data from areas of most severe histological distortion in distal small intestine of mice two days post final tamoxifen injection. For immunofluorescence, each data point is the mean of three representative sections imaged per mouse with bars at median value. Scale bar 100 μ M.

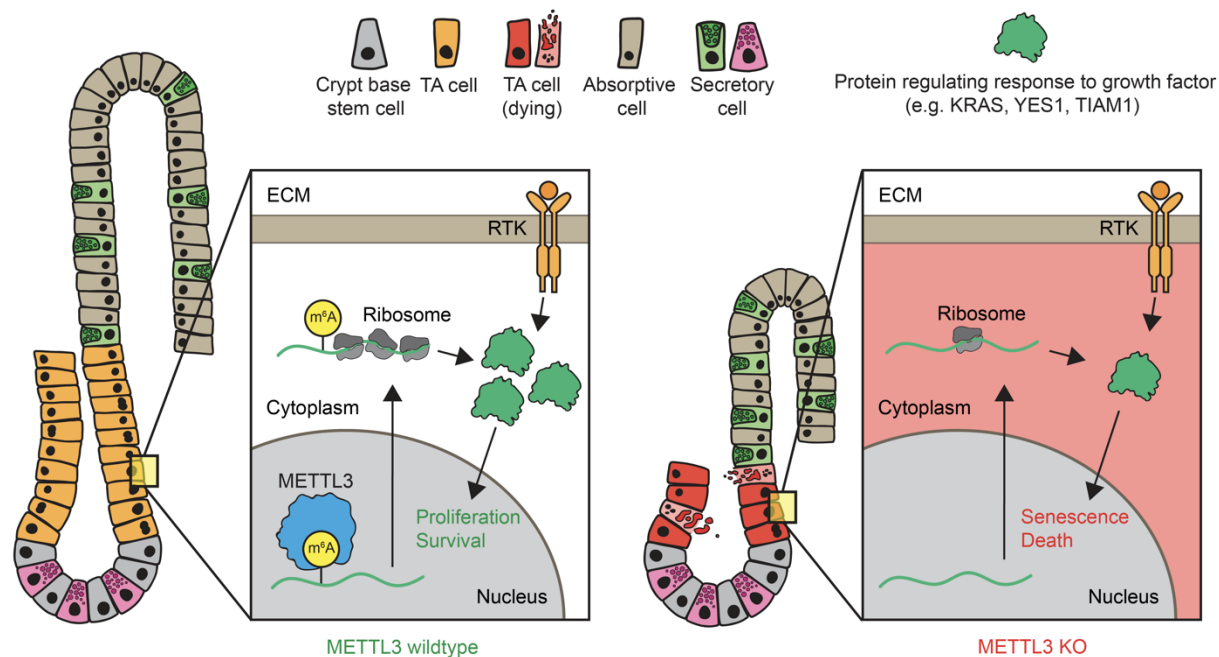


Figure 8. METTL3 maintains growth factor signaling and survival in intestinal transit amplifying cells. Proposed model. In wildtype mice, METTL3 methylates *Kras* and other transcripts involved in transducing growth factor signaling. Methylation promotes translation of these transcripts, enhancing proliferation and survival in transit amplifying (TA) cells downstream of external growth factors. In the absence of METTL3, a decreased response to extracellular growth factors in METTL3 knockout TA cells leads to cellular senescence and death. Loss of transit amplification results in reduced crypt and villus size and diminished production of absorptive cells. ECM, extra cellular matrix. RTK, receptor tyrosine kinase. Green protein represents KRAS and other proteins regulating the intracellular response to growth factors.